



Experimental Study of Failure and Morphology of Large Granite Specimens Under Confining Pressure and Blast Loading

Jiazheng Gao^{1,2,3} · Yeqing Chen^{2,3} · Zhenqing Wang¹ · Yongsheng He^{2,3} · Chunhai Li²

Received: 22 December 2023 / Accepted: 29 August 2024

© The Author(s), under exclusive licence to Springer-Verlag GmbH Austria, part of Springer Nature 2024

Abstract

In this study, we examined the influences of high in-situ stress and blast loading on granite within deep-tunnel excavation and mining contexts. A large granite specimen ($1200 \times 1200 \times 200 \text{ mm}^3$) was subjected to chemical explosion tests under varying confining pressures. The entire granite failure process was visualized using high-speed photography, and a damage characterization method based on three-dimensional scanning technology and digital model reconstruction technology was developed. The failure mode of the granite was divided into three distinct stages: the crushing failure stage, circumferential fracture stage, and stepped fracture stripping stage. Microscale examination of the fracture surfaces revealed the presence of sharp, step-like structures with pronounced directional characteristics. A key finding is the significant variability of the explosion crater features under different confining pressures. Vertical stress significantly impacted the volume of the crater and the area of the damage zone on the granite's surface, exhibiting a positive correlation and elliptical morphology aligned with the static stress direction. Under constant vertical stress, the horizontal stress played an inhibiting role in the failure of the back surface of the granite, leading to a morphological shift from elliptical to nearly circular in the damage zone. Under equal biaxial stresses, a low static stress promoted crushing of the granite, while a higher static stress restrained it. In this study, it was found that under different stress states, the equivalent diameter of the crater was much larger than its average depth, and the morphology of the crater profile exhibited a flat funnel-like shape with ladder-shaped fracture patterns.

Highlights

- Conducts experiments on large granite specimens under complex stresses to study their damage, fracture process, and morphological characteristics.
- Introduces a novel damage characterization method using 3-D scanning and digital modeling to analyze granite's post-explosion morphology.
- Granite specimens' failure occurs in three stages: the crushing failure stage, circumferential fracture stage, and stepped fracture stripping stage.
- Extracts and calculates granite crater's post-explosion parameters, revealing morphology changes under complex stresses.

Keywords Large granite specimen · Confining pressure · Blast loading · Fracture morphology · 3-D laser scanning

✉ Zhenqing Wang
wangzhenqing@hrbeu.edu.cn

✉ Yongsheng He
hyshyb2023@163.com

¹ College of Aerospace and Civil Engineering, Harbin Engineering University, Harbin 150001, China

² Institute of Defense Engineering, AMS, PLA, Beijing 100036, China

³ State Key Laboratory of Target Vulnerability Assessment, Beijing 100036, China

1 Introduction

With the gradual exhaustion of shallow resources, the progress of underground engineering construction technology, the development of deep drilling technology, and the different needs of researchers in the fields of life sciences, geophysics, deep-underground medicine, deep-rock mechanics, and other disciplines (Ranjith et al. 2017; Roszkowski et al.

2018; Liu et al. 2018), an increasing number of underground engineering projects have gradually developed from shallow to deep (Chazal et al. 1998; Miuchi et al. 2003; Alner et al. 2005; Lesko 2009; Hu et al. 2011; Lippmann-Pipke et al. 2011; Feng et al. 2015; Zhao et al. 2017; Parisi et al. 2017). At present, the drilling and blasting method is still the main means of rock excavation and is widely used in tunnels, mining, and other projects (Rustan 1998; Yilmaz and Unlu 2014; Yan et al. 2015). In contrast to surface rocks, high in-situ stress is one of the main characteristics of deep-rock masses (Saiang 2010; Kulatilake et al. 2013). Compared with shallow engineering, under the influence of the in-situ stress in deep engineering, the initial stress field of the surrounding rock is redistributed during blasting, resulting in over- or under-excavation, collapse, rockburst, and other disasters (Gong et al. 2012; Li et al. 2012, 2017; Yan et al. 2015; Zhao et al. 2017). These factors significantly affect the effectiveness of rock blasting. It is of great importance to study the blasting fragmentation characteristics of rock masses under different confining pressures and blast loads to improve the effectiveness of blasting, increase the efficiency of rock blasting excavation, and ensure the safety and efficiency of production. This problem has attracted the attention of many scholars (Kutter and Fairhurst 1971; Jung et al. 2001; Yang and Ding 2018).

Research on the characteristics of the rock mass explosion failure process, the morphological characteristics of the resulting crater, and the many influencing factors is very complex. Some of the most important factors are the non-linear, dynamic, and transient behavior of the explosion load, which have the characteristics of a high amplitude and high frequency (Goel and Matsagar 2014). Nordyke (1961) was the first to derive the main mechanisms and preliminary theories of the formation of explosion craters by summarizing and analyzing the results of four nuclear explosion tests conducted at the Nevada Test Site. Sher et al. (2011) studied the explosive effect on rock masses near the free surface, and based on the theory of linear brittle fracture, they established a kinematic calculation model of a crack that initiated at the center of the explosion and extended to the free surface. Chi et al. (2019a) investigated the fragmentation of six granite samples ($400 \times 400 \times 400 \text{ mm}^3$) under different blast loads. On this basis, Chi et al. (2019b) investigated the influence of radial constraints on the expansion and fracture patterns of granite columns and determined the relationship between the peak pressure of the shock wave and its damping index by analyzing data from sensors embedded in the specimen. Their results provide an effective reference for verification of the numerical rock blasting model. He et al. (2020) studied the mechanisms of rock rupture caused by single-hole to multi-hole blasting using a high-speed camera and strain measurements to measure the crack extension and strain field in granite materials under the effect of blasting, respectively.

Deep underground mining is influenced by the high in-situ stress. In recent years, the influence of a high in-situ stress on the blasting fragmentation of a deep-rock mass has become a growing concern for many scholars and engineers (Yang et al. 2017, 2018; Yi et al. 2018; Xie et al. 2019, 2021; Wu et al. 2022). Zhang et al. (2017) used cement mortar to prepare rock model materials and studied the explosive crushing phenomenon of rock-like materials under different uniaxial and biaxial confining pressures. Peng et al. (2019) also used cement mortar to simulate rock materials and studied the failure behavior characteristics of rock under high-stress conditions employing a self-developed electrical explosion system. Their experiments revealed that the static stress field is a significant factor affecting the internal strain field of the specimen, which in turn affects the crack propagation behavior of the specimen and the final morphology of the crater. He and Yang (2018a) developed a dynamic and static loading device that can simulate the in-situ stress conditions by providing pressure through a hydraulic device and analyzed the rock strain field and crack extension under confining pressures of 0 MPa, 5 MPa, and 10 MPa. Their test results revealed that rock fractures are mainly generated via tensile and shear failure, and the circumferential compressive stress reduces the circumferential tensile failure under a blasting load. Therefore, the radius of the rock fracture zone decreases with increasing confining pressure. He et al. (2018) also analyzed the damage patterns caused by different K values (ratio of the horizontal to vertical confining pressure) of rocks under a blasting load. They found that the radius of the damage zone produced by an explosion on the free surface and the radius of the crack gradually decreased with increasing K . Based on the above study, He and Yang (2018b) successfully applied the Johnson–Holmquist (JH) damage constitutive model in AUTODYN two-bit code to verify the above conclusions. Yang et al. (2021) simulated the blasting failure characteristics of a rock mass under different confining pressures by applying horizontal and vertical loads to gypsum specimens and discussed the influences of the magnitude and direction of the in-situ stress on pre-splitting blasting.

The drilling and blasting methods are still widely used in mining and tunnel excavation processes, and the rock mass is affected by the combined effect of the in-situ stress and explosion during the excavation process. Numerous scholars have conducted experimental research on the mechanical failure characteristics of rocks under the combined effect of the confining pressure and explosion. Due to the difficulty of finding, mining, and processing large rocks that meet the experimental conditions, as well as the limitations of the related testing equipment, current research has mainly focused on theoretical analysis, numerical simulations, model materials, and small-scale rock specimen testing. Few

experimental studies have directly tested large raw granite specimens.

Regarding the experimental materials, compared with rock simulating materials, using an actual rock has more advantages. First, an in-situ rock mass can truly reflect the natural physical and mechanical properties. This means that the obtained experimental data can more accurately represent the response of real rocks. Second, extensive research has shown that the microstructure of the material determines its macroscopic mechanical properties (Exadaktylos and Vardoulakis 2001; Lan et al. 2010; Chen et al. 2017; Peng et al. 2018). The rock itself is generally a solid mixture of various minerals, and a large number of irregular pores and structural planes of different scales are distributed inside the rock. These structures may affect the response of the rock under dynamic loading. Rock-like materials are generally composite materials that are composed of cementitious materials that bond aggregates into a whole specimen. Although for certain characteristic parameters, adjusting the aggregate ratio can maintain consistency with rock materials, their different internal structures inevitably lead to the occurrence of different fracture failure characteristics under the combined effect of an explosion and the confining pressure. In addition, the natural heterogeneity of the original rock can have an impact on its mechanical behavior, especially under dynamic loading. The original rock may exhibit complex failure modes related to its structure and composition. In contrast, rock-like materials are relatively uniform and cannot accurately reproduce the failure modes of rocks characterized by heterogeneity. Finally, in engineering applications such as tunnel blasting and seismic engineering, the data and patterns obtained using original rocks are more practical and effective, because they reflect the behavior of real rocks.

In terms of the size of experimental samples, the mechanical properties of large rock samples under different loading conditions are currently an important research direction for analyzing rock mechanics. Research on the mechanical properties of large rock specimens has received increasing attention from scholars (Guo et al. 2012; Xia et al. 2014; Cheng et al. 2020). A rock is a heterogeneous and anisotropic material with significant size effects (Weibull 1939, 2013; Hudson et al. 1972; Masoumi et al. 2016), and the mechanical properties and failure modes of rock masses of different scales can vary greatly (Meng et al. 2016; Chen et al. 2018a; Kao et al. 2020; Wu et al. 2021; Ai et al. 2021; Qi et al. 2023). Lu et al. (2007) pointed out that when the sample size is greater than 70 mm × 210 mm, the fracture characteristics of the specimen gradually stabilize under loading, and they proposed a size-effect parameter based on this size as a standard. The process of rock fracturing actually consists of the expansion and combination of internal micropores and microcracks, and some studies have shown

that the expansion of rock fractures also has scale effects (Wei et al. 2017; Zhang et al. 2019, 2021). Larger specimens contain more internal structures, such as microcracks, interlayers, and other discontinuous surfaces. Moreover, due to their larger volumes, larger specimens provide a better statistical representation of the rock's properties, which may not be evident in smaller specimens. As the sample size increases, the dispersion of the mechanical properties of a fractured rock mass decreases, and the mechanical properties of the rock mass become increasingly stable (Bear 1975). Furthermore, the use of a large-scale granite model greatly reduces the influences of boundary effects. Therefore, regarding engineering applications such as tunnel blasting or mining engineering, under the combined effects of different confining pressures and explosive load conditions, large granite specimens can more accurately reflect the true fracture characteristics of in-situ rock masses. With the development of rock mechanics and the improvement of the experimental level, it is necessary to conduct tests on the damage characteristics of large granite specimens under complex stress field conditions to study the rock's damage and fracture processes and failure morphology characteristics.

In terms of the selection of an explosion source, many studies have adopted the method of replacing chemical explosions with electric explosions due to safety and cleanliness considerations (Lisitsyn et al. 1998; Yan et al. 2016, 2019; Guo et al. 2019; Peng et al. 2019, 2020a, b). However, compared with electric explosions, chemical explosions have more significant advantages in terms of the energy output, explosion range, and duration. First, in terms of the energy output, chemical explosions often have a greater energy output and rapidly release a large amount of heat and gas, while electrical explosions have a lower energy output. Second, chemical explosions can generally affect larger areas and can generate larger shock waves and explosion effects, which are very important in engineering and research on the dynamic mechanical properties of large-scale rock masses. In addition, chemical explosions can last for a longer period of time, while point explosions typically have a shorter duration. At present, chemical explosions are still the main method utilized in the fields of mining, tunnel engineering, construction, and military engineering. Therefore, as an explosion source, chemical explosions are closer to the actual engineering situation and can reflect the real dynamic mechanical behaviors of rocks.

In summary, the current research has shown that the confining pressure is the main factor affecting the morphological characteristics of rock explosion failure. However, experimental studies have mostly utilized rock-like materials or small granite specimens or have used electric explosions instead of chemical explosions. A few studies have conducted chemical explosion tests on large raw granite

specimens under different confining pressure conditions. In this research context, to study the failure process and post-explosion morphology characteristics of granite under the combined effect of the confining pressure and explosion, indoor chemical explosion tests were conducted on large granite samples under different confining pressures. In the experiment, high-speed photography was used to visualize the entire process of granite failure, and after the experiment, 3-D laser scanning measurement technology was used to obtain the characteristic parameters that can describe the morphology of the blast crater. In addition, based on three-dimensional coordinate data and digital model reconstruction of the damage characteristics, we developed a method for characterizing the morphological characteristics of the blast crater. Via the above technical means, the failure process and post-explosion morphological characteristics of large granite specimens under the combined effect of the confining pressure and explosion were analyzed. The results of this study provide a certain reference for research on the size effect on the explosion morphology characteristics of granite under different loading and explosion conditions.

2 Materials and Methods

2.1 Rock Material

The granite samples utilized in the experiment were sourced from Shandong, China, at a depth of 410 m. Because the natural rock mass was non-homogeneous, to ensure the accuracy and representativeness of the test data, all of the granite

samples were collected from the same parent rock, and water drilling technology was used to cut the rock to avoid the development of surface or internal crack defects caused by processing vibrations. The parameters of the granite were as follows: density of 2.6 g cm^{-3} , Poisson's ratio of 0.18, Young's modulus of 26.4 GPa, tensile strength of 12 MPa, and compressive strength of 115.8 MPa. Split-Hopkinson pressure bar (SHPB) tests were conducted to measure the dynamic compressive strength of the granite, which was found to be 151.4 MPa, at a strain rate of 115 s^{-1} , loading speed of 8.081 ms^{-1} , and loading pressure of 0.4 MPa. The microstructure of the granite was observed via scanning electron microscopy (SEM) (Fig. 1).

Through X-ray diffraction (XRD) whole-rock mineral quantitative analysis (Table 1), the main minerals in the granite specimens used in this test were determined to be plagioclase (49.7% on average) and quartz (23.2% on average).

2.2 Specimen and Blasting Parameter Design

To simulate the mechanical response of the rock mass under real conditions at depth, six granite blocks with dimensions of $1200 \times 1200 \times 200 \text{ mm}^3$ were selected, and six different confining pressures were applied. The specific test scheme is shown in Table 2. Figure 2 shows the geometric size and charge structure of the specimen. The borehole was located in the center of the granite. The specimen was drilled to a depth of 160 mm, the bottom of the hole was 40 mm from the exposed surface, and the diameter of the hole was 20 mm.

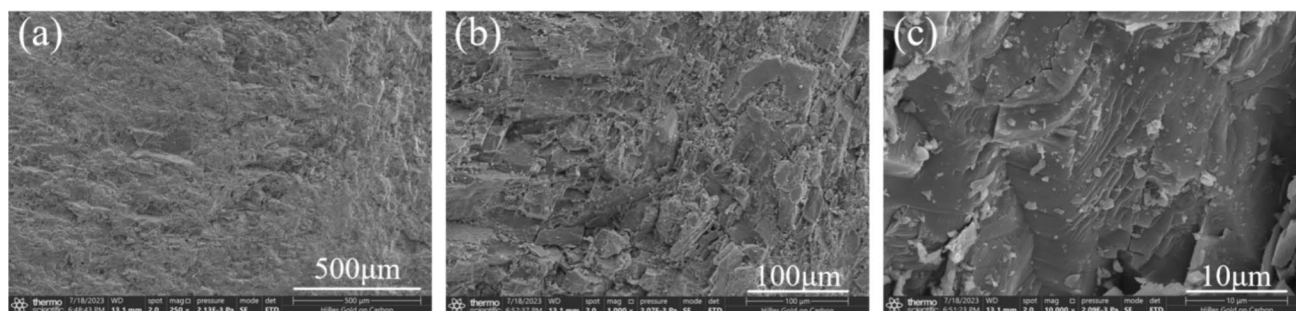


Fig. 1 SEM images of the free surface of the granite specimen before testing

Table 1 Quantitative XRD data for the whole-rock minerals

Specimen	Mineral contents (%)					
	Quartz	Plagioclase	Potassium Feldspar	Mica	Chlorite	Amphibole
1	24.2	50.1	14.8	9.1	0.7	1.1
2	23.2	50.3	13.2	12.8	0.5	–
3	22.4	48.8	11.8	16.5	0.5	–

Table 2 Size of the test specimen and stress application conditions (σ_h is the horizontal pressure, σ_v is the vertical pressure, and $K = \sigma_h/\sigma_v$)

Specimen	Size of specimen (mm ³)	σ_v (MPa)	σ_h (MPa)	K
HGY-1	1200×1200×200	0	0	–
HGY-2	1200×1200×200	4	0	0
HGY-3	1200×1200×200	8	0	0
HGY-4	1200×1200×200	8	4	0.5
HGY-5	1200×1200×200	4	4	1
HGY-6	1200×1200×200	8	8	1

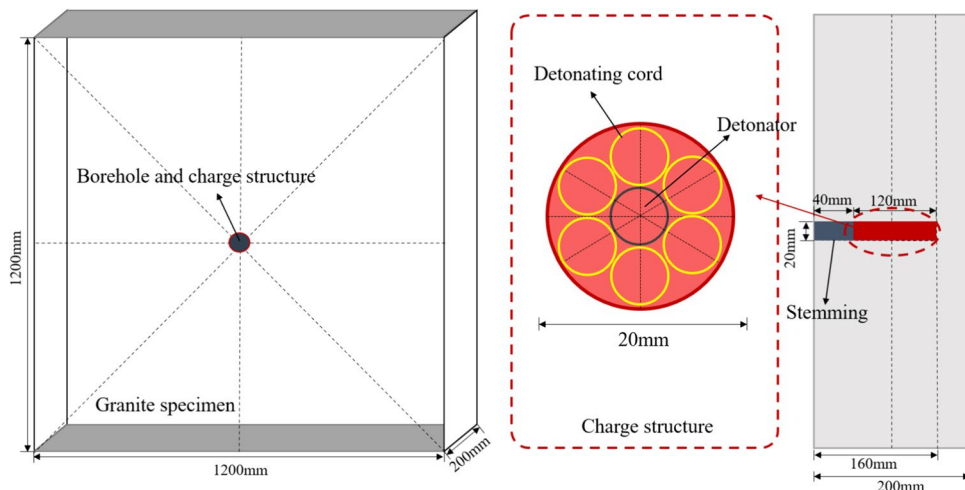
As shown in Fig. 3, the charge structure in this test was composed of a high-precision electronic detonator and a No. 5 coal mine detonating cord. The charge structure consisted of a detonator in the center and six detonating cords evenly

distributed around it. The length and diameter of each detonating cord were 120 mm and 6.5 mm, respectively, the length and diameter of the electronic detonator were 80 mm and 6.5 mm, respectively, and the total length of the charge was 120 mm. After the charges were tied, they were placed in the borehole, and the charges were fully attached to the borehole wall, creating a coupled charge structure. After the charges were placed, the blasthole was sealed with fast-setting C30 concrete. In this test, the explosive charge was the equivalent of 12.6 g TNT, and the electronic detonator was detonated using a special hand-held electronic detonator initiator. The blasting charge remained unchanged.

2.3 Equipment and Test System

To study the explosive failure behavior of the rock mass under different confining pressures (Fig. 4), during the

Fig. 2 Size of the specimen and charge structure



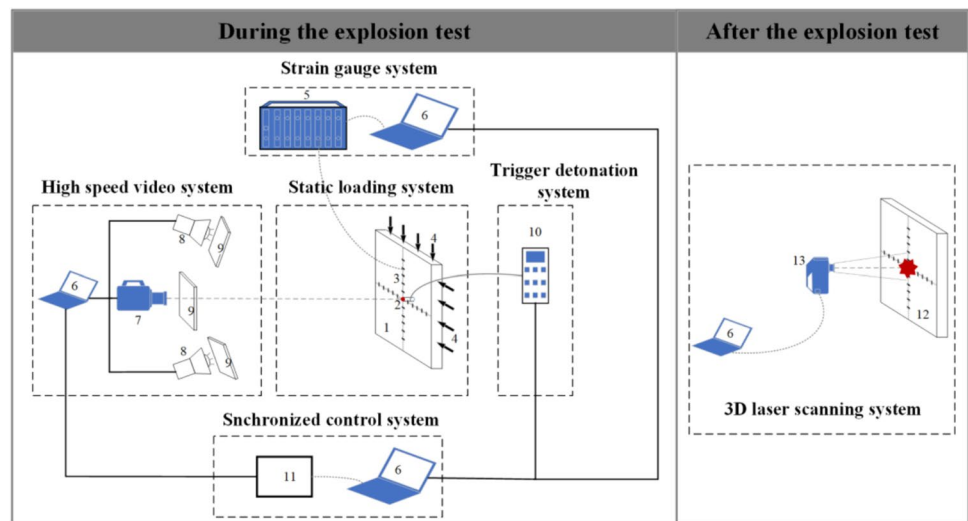
(a)



(b)

Fig. 3 Electronic detonator and detonating cord: **a** high-precision electronic detonators; and **b** detonating cord

Fig. 4 Diagram of the testing system. 1—granite specimen, 2—blastholes, 3—strain sensor, 4—static load, 5—data acquisition instrument, 6—computer, 7—high-speed camera, 8—light source, 9—protective glass, 10—hand-held electronic detonator, 11—delay synchronization controller, 12—granite specimens after the explosion, and 13—three-dimensional laser scanner

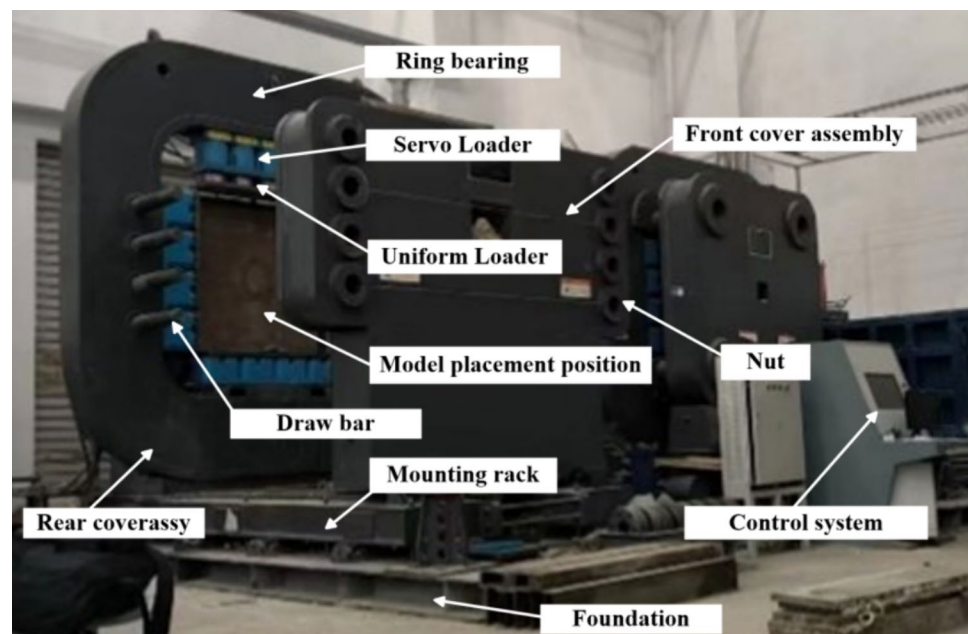


explosion test, the entire testing system consisted of a static loading system that applied the static stress, a trigger initiation system, a high-speed camera measurement system, a strain data acquisition and analysis system, and a synchronous control system. After the test, the post-explosion granite specimens were scanned and measured using a three-dimensional laser scanner.

The static loading system in the testing system was the whole process simulation testing system of deep-underground engineering structure instability (Fig. 5). The granite was placed in the model placement position, and the stress was applied according to the designed scheme (Table 2) after the placement was completed. The servo loading device enabled the load to be applied and

maintained independently in the horizontal and vertical directions. The stress was applied using a graduated loading method. The granite specimen was placed in the chamber of the testing equipment, and the confining pressure was incrementally increased to $1/7$ of the preset stress at a constant loading rate. This was followed by a stabilization period of 10 min, which completed the first loading stage. The second stage involved increasing the confining pressure to $2/7$ of the preset stress at the same loading rate. This was followed by another 10-min stabilization period. This process was repeated through seven stages until the confining pressure reached the designed value. After the loading was completed, the specimen was stabilized for 1.0–1.5 h, and the explosive was detonated after

Fig. 5 Experimental equipment



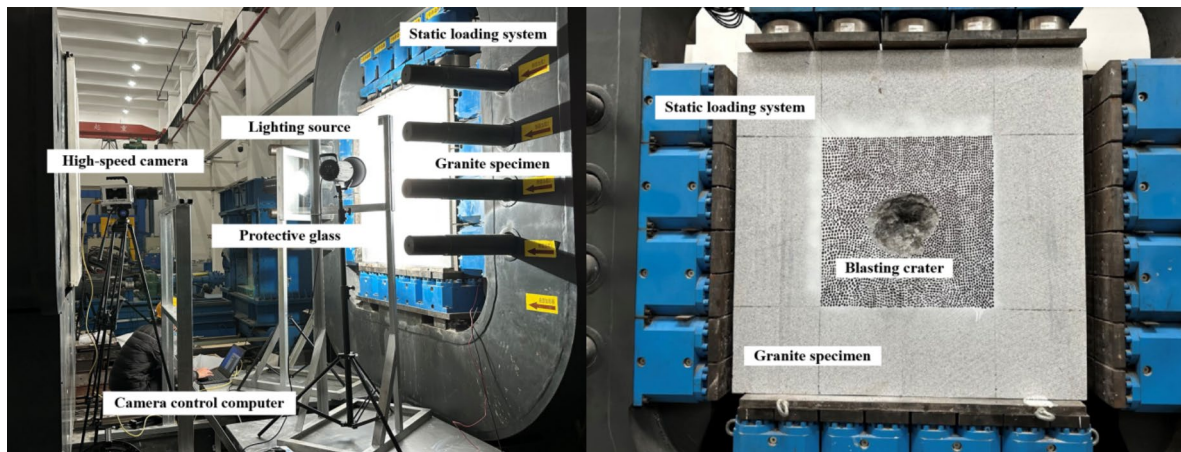


Fig. 6 Field test arrangement and image of the specimen after the explosion

completion of the pressure stabilization process. Figure 6 shows the set-up of the test and the failure morphology of the granite specimen after the explosion.

To more intuitively and accurately obtain the shape, area, depth, and volume of the crater after the explosion and to further study the morphological characteristics and damage evolution of the blast damage, it was necessary to accurately measure the characteristic parameters of the crater morphology. Because granite is a heterogeneous anisotropic material, the shape of the crater and the crack distribution were extremely irregular after blasting. Therefore, direct measurement of the granite specimens after blasting could not provide comprehensive and high-precision data for the geometric features, and the relevant parameters could not be accurately measured. Wang et al. (2018) poured molten paraffin into the crater and removed it after it cooled to obtain the characteristic parameters of the crater by measuring the mold of the crater. This method has certain errors, and the operation process is more complicated. With the continuous development of measurement technology, computed tomography (CT), the digital image correlation (DIC) method, three-dimensional (3-D) laser scanning measurement technology, and other non-contact measurement methods have been gradually applied in relevant experimental rock mechanics research (Chen et al. 2018b; Chi et al. 2019a; Fan et al. 2020a, b; Yang et al. 2021; He et al. 2021; Gao et al. 2021). Three-dimensional scanning can accurately obtain the three-dimensional coordinate data for the damage morphology of the rock and can construct a three-dimensional digital model of the crater morphology. The crater damage parameters can also be extracted from the reconstructed digital model. In this study, a hand-held 3-D scanner (Artec 3-D scanner) was used to obtain 3-D point cloud data with an accuracy of 0.1 mm, a maximum 3-D resolution of 0.5 mm, and a 3-D reconstruction rate of 16 frames per

second. Multi-angle scanning was performed at a distance of 10–20 cm from the surface of the post-blast granite specimen. The three-dimensional point cloud data for the entire granite specimen after blasting were obtained via three-dimensional laser scanning.

3 Experimental Results

3.1 Failure Process and Failure Mode of Explosion Crater

The frame rate of the high-speed camera used in the test was 500,000 fps, and the failure mode of all of the granite specimens was roughly the same under the different test conditions. Figure 7 shows the failure evolution process of the granite specimens using condition HGY-2 as an example. At 200 μ s, the surface of the granite specimen exhibited a bulge, and a ring of circumferential cracks formed around the circular bulge. The velocity of the stress wave propagating on the surface of the specimen was much greater than that of the explosive gas, so overflow of the blasting dust was not observed after the formation of the circumferential crack. At 300 μ s, the bulge was further uplifted under the action of a free surface stress wave, and the granite at the edge of the bulge reached its ultimate tensile strength, resulting in the formation of a small network of cracks around the bulge. This process was accompanied by an explosion of gas and dust overflowing from the small cracks in the fracture zone. At 400 μ s, the circumferential cracks generated around the bulge of the granite were completely developed and closed. The granite block within the circumferential crack had been completely separated from the specimen and thrown out as a whole piece. In addition, the second circumferential crack gradually formed and extended, and most of the blasting dust overflowed in the fractures generated by the second

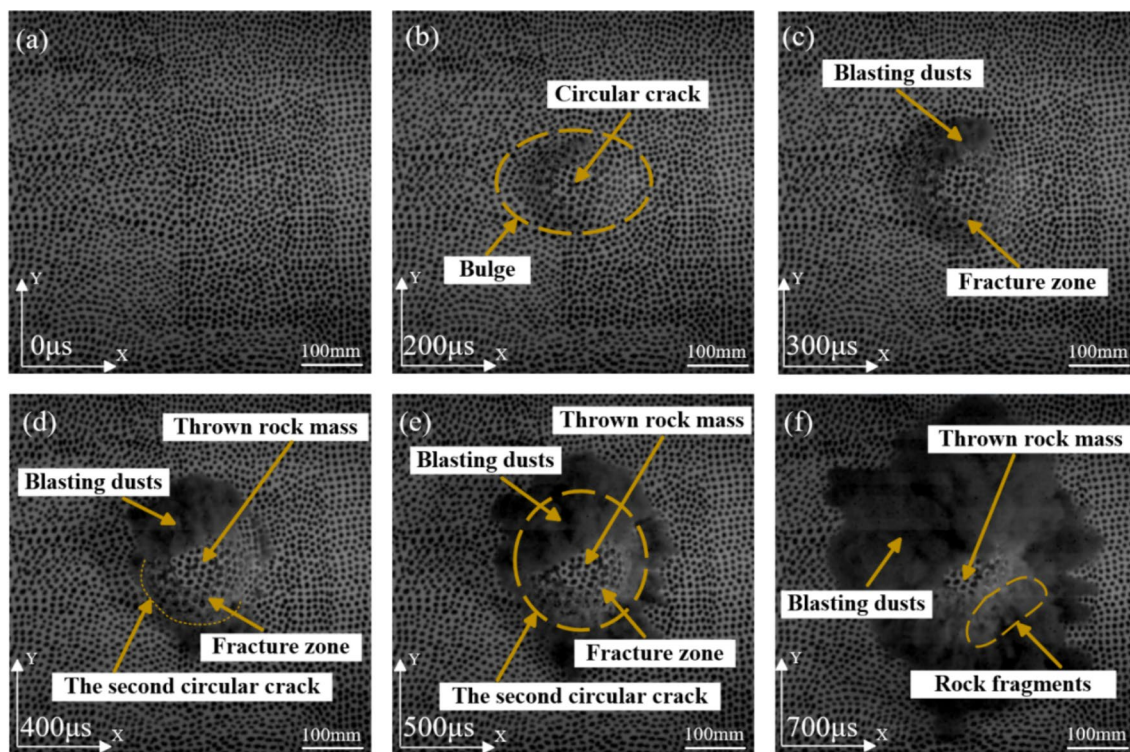


Fig. 7 Typical failure process of the back of a granite specimen

circumferential crack. At 500 μs , the second circumferential crack was completely closed. Under the combined action of the stress wave and bursting gas, larger granite blocks peeled off and were thrown out, accompanied by more small fragments shooting out and the escape of blasting dust. At 700 μs , the surface of the granite specimen was completely broken. During this process, the spalled rock fragments were completely thrown out, and the second circumferential crack gradually developed and formed the boundary of the blast crater. In the typical failure process of granite, the energy and initial velocity acquired by the rock under the action of a compression wave and the free surface stripping phenomenon caused by the reflected tensile wave play dominant roles in the formation of craters (Hagan 1979; Wang et al. 2007; Peng et al. 2019; He et al. 2020).

Throughout the explosion process, the granite medium was in an extremely complex stress state. The granite underwent crushing, uplift, spalling, and throwing processes, culminating in the formation of a blast crater. Based on the macroscopic characteristics, the failure mode of the granite specimen was divided into three stages: the crushing failure stage, circumferential fracture stage, and stepped fracture stripping stage. The first stage was the crushing failure stage (Fig. 7a, b), which mainly occurred at the bottom of the entire crater. The granite was severely fractured and deformed by the extrusion caused by the explosion, and the interior of the rock mass was crushed

or even powdered. When the blast compression wave did not reach the free surface, the law of medium motion and damage was similar to that of a closed explosion (Nordyke 1961; Kutter and Fairhurst 1971; Sher et al. 2011). After the compression wave reached the free surface, the evolution of the crater caused by the explosion was symmetric before the reflected relief wave reached the crater caused by the explosion. However, due to the shallow depth of the explosive charge and the use of non-penetrating drilling, the asymmetric development of the crater occurred in the initial stage. The reflection of the compression wave from the free surface caused spalling of the rock mass. The damage zone was uplifted at the free surface and caused the formation of a bulge on the surface of the specimen. In addition, a circumferential fracture zone formed around the bulge. The second stage was the circumferential fracture stage (Fig. 7b, d, e). In this stage, the stress wave reached the free surface and produced a reflected tensile wave. An approximately circular area of tensile strain concentration was formed around the center of the granite. The tensile strain also increased continuously with time. When the ultimate dynamic tensile strength of the granite was reached, circumferential fractures formed in the free surface. Under the propagation of the stress wave on the surface of the granite specimen and the impulsive wedge effect of the bursting gas, the circumferential fracture continued to extend, and eventually, the outermost

circumferential fracture formed the boundary contour of the crater. The third stage was the stepped fracture stripping stage (Fig. 7d–f). This stage took place after the circumferential crack was fully developed. Under the rarefaction of the waves at the free surface and the internal shock waves, the granite underwent laminar fracturing, and pieces were thrown out. The final morphology of the crater was not a wide funnel shape with a smooth transition. Instead, the crater wall had a distinct ladder-shaped fracture and irregular rough surfaces.

Based on this, the characteristics of the formation process of the crater caused by the explosion in the large granite specimen were significantly different from those of rock-like materials prepared using concrete and cement mortar with a certain mixing ratio. This was mainly reflected in three aspects. First, obvious radial tensile cracks formed in the rock-like materials during the initial stage of the explosion (Peng et al. 2020a, b). In contrast, obvious cracks did not form in the large granite specimen in the initial stage, and it directly bulged and subsequently produced circumferential cracks. This occurred, because the stress wave that propagated outward from the center of the explosion during the initial stage was initially a compression wave. Subsequently, when the wave propagated to the free surface, it was reflected and transformed into a tensile wave. The bonding interface between the aggregates and the cement matrix near the free surface of the rock-like materials became a weak point for fracturing, resulting in the formation of tensile cracks (Zaitsev and Wittmann 1981; Sharma and Bishnoi 2019). Due to its high density and uniform structure, the granite underwent uplift when subjected to compressive stress. The damage caused by the reflected tensile waves mainly occurred in the stress concentration zone at the boundary of the uplifted part of the granite, resulting in the formation of circumferential fractures. The failure process of the rock-like material under an explosion was a process of overall fragmentation and throwing out of material, and the final crater was funnel-shaped (Zhang et al. 2017; Wang et al. 2018; Peng et al. 2019, 2020a, b). However, the granite exhibited varying degrees of anisotropy due to the distribution and orientation of the different minerals within it. These structural differences made the stress waves more prone to failure at certain levels, leading to delamination and fracturing. Finally, compared with the rock-like materials, larger and more complete blocks were thrown from the granite. From a microscopic perspective, there were more microdefects such as micropores and microcracks inside the concrete, and there were a large number of bonding interfaces between the aggregates and the cement-based materials. These defects caused the internal crack propagation paths in the rock-like materials to be more extensive, making it easier to produce small fragments.

In contrast, the granite was composed of closely bound mineral grains, and the cracks between the dense mineral grains were easily hindered during the propagation process, resulting in limited crack propagation and the throwing out of larger fragments during the explosion process.

3.2 Failure Morphology Characteristics Under the Combined Effect

The granite usually exhibited different morphological characteristics after the explosion due to its inhomogeneity, brittleness, and low tensile strength. By analyzing the morphology of the blast crater, the extent of the explosion damage and the influence of the different confining pressures on the cratering were qualitatively analyzed and evaluated. HGY-1-1 represents the plane where the blasthole was located in the granite (front) under the first set of working conditions. In HGY-1-2, the blasthole in the granite (back) did not penetrate the plane under the first set of working conditions, and so on. A total of 12 sets of typical failure morphology features were measured for each granite specimen under the six different sets of working conditions on the front and back surfaces.

Figure 8 shows the failure morphology characteristics of the granite specimens after blasting. It can be seen from Fig. 8 that there were obvious crushing zones, a spalling platform, and spalling cracks around the explosion crater. Based on the above analysis of the failure process and failure mode of the granite, during the blasting process, spalling cracks developed near the granite crushing zone and closed in the initial stage of the explosion, which led to peeling and throwing out of the block under the action of the shock wave. The second circumferential spalling crack was developed and closed under the combined effect of the reflected tensile waves and the impulsive wedging effect of the bursting gas on the rock fractures, and a distinct spalling platform developed between the two circumferential spalling cracks. Figure 9 presents three-dimensional profiles of the explosion craters. It can be seen that each profile of the blast crater contained a ladder-shaped fracture, which was distinctly different from the morphology of the rock-like material after blasting (Zhang et al. 2017; Wang et al. 2018; Peng et al. 2019, 2020a, b).

After the experiment, samples were collected from the surface of the granite explosion crater for SEM observation at different magnifications (Fig. 10). As can be seen from the SEM image magnified 20,000 times, the fracture surface exhibits a clear stepped fracture structure, and the edge of the fracture is relatively sharp, indicating that it is a brittle fracture caused by the impact of the explosive. Furthermore, during the propagation process, the stress waves were prone to diffuse along the internal structural planes of the granite, resulting in the obvious directionality of the

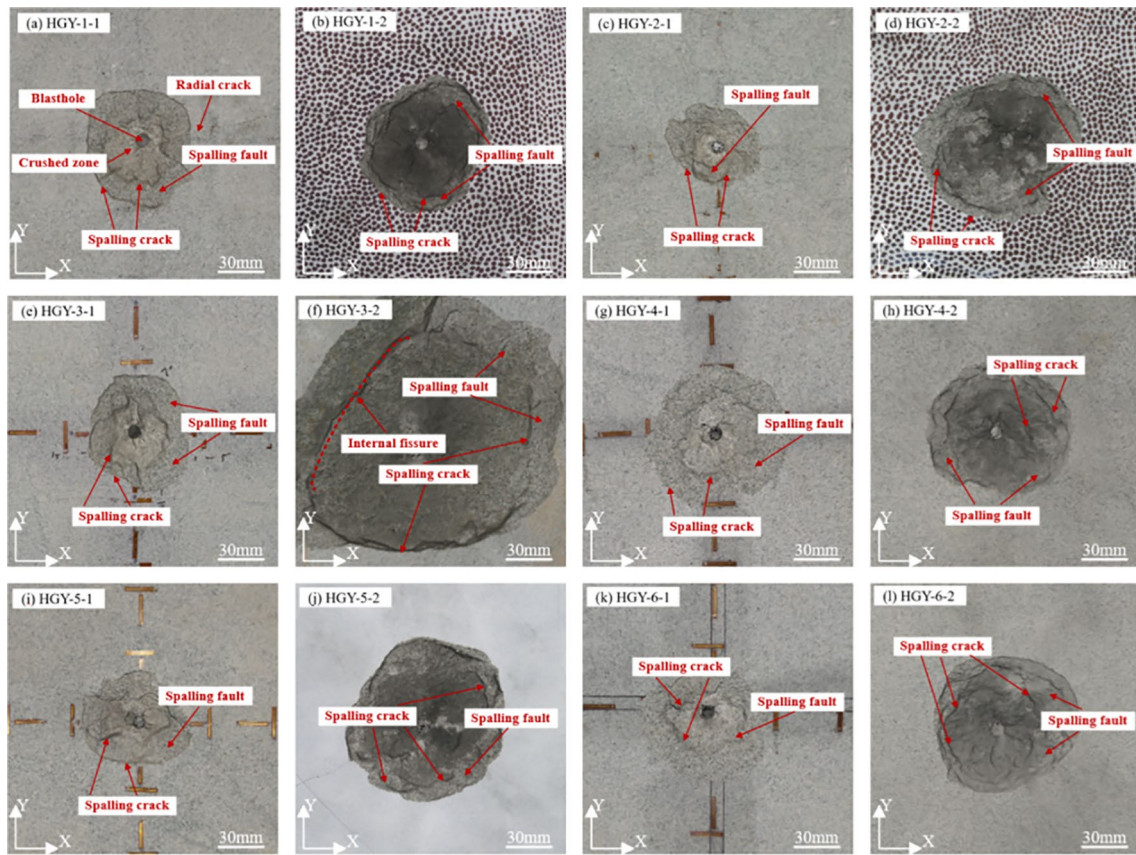


Fig. 8 Post-explosion failure morphology characteristics of the granite specimens

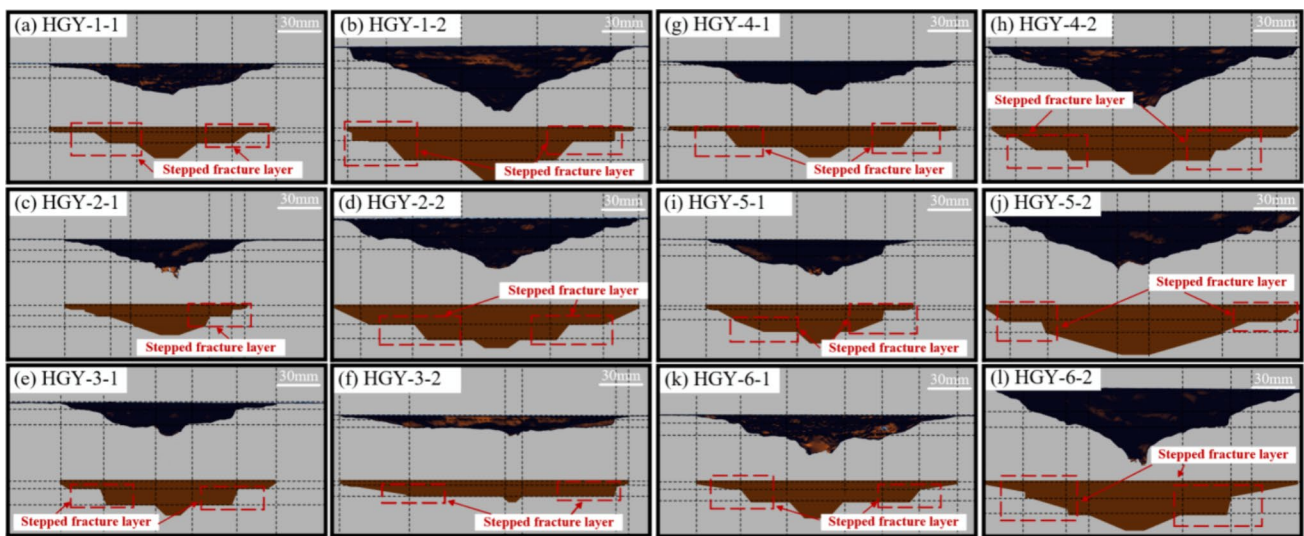


Fig. 9 Three-dimensional profiles of the blast craters in the granite specimens

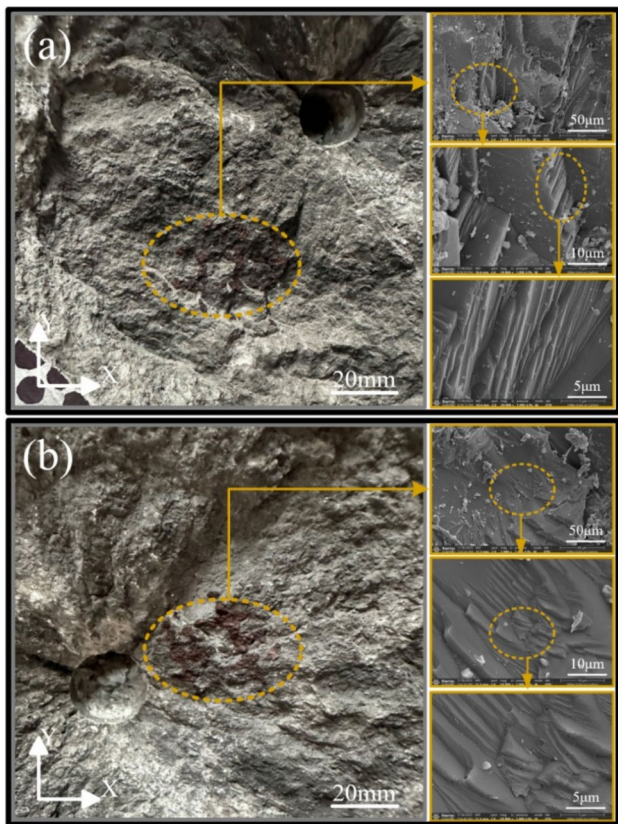


Fig. 10 SEM images of the morphology of the damage to the surface of a blast crater (Taking HGY-1-2 as an example). **a, b** Present images of two different sampling positions in HGY-1 and HGY-2, respectively

fracture surface shown in Fig. 10. In the images acquired under smaller magnification, debris can also be observed on the fracture surface. This is because the explosion created internal and intergranular fractures in the crystals, resulting in smaller mineral particles being removed due to fracturing and friction.

3.3 Construction of a Digital Crater Model and Method of Characterizing the Crater Morphology

Three-dimensional laser scanning measurement technology was used to measure the surface of the granite, and the angle and distance of the emitted laser determined using the received reflection signal were recorded to determine the spatial coordinates of each point on the granite, thereby creating a point cloud of the geometric surface. This process was used to digitize the three-dimensional features of the surface of the rock specimen after blasting. In addition, these dense point clouds were used to generate the shape of the surface of the specimen and to construct a three-dimensional digital model of the granite after blasting. The digital model accurately describes the shape and size of the crater after blasting and was used to accurately calculate the surface area, volume, depth, and location of the crater.

To construct the three-dimensional digital model of the granite after the explosion, data registration, noise reduction, gross errors, redundant data elimination, data analysis, and surface fitting were performed on the point cloud data obtained via scanning, and finally, a three-dimensional

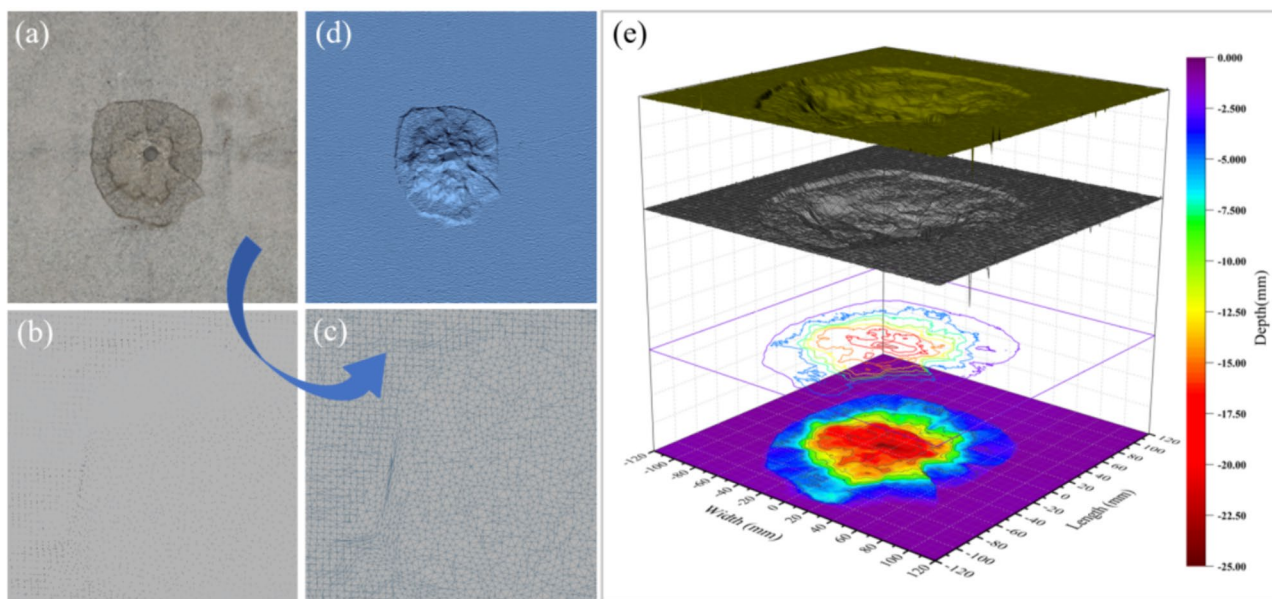


Fig. 11 Diagram showing the processes of three-dimensional digital modeling and three-dimensional digital elevation model establishment: **a** blast crater in granite specimen, **b** point cloud data model, **c**

three-dimensional mesh model, **d** constructed three-dimensional digital model, and **e** Digital elevation cloud map

digital model of the granite was generated. Subsequently, by processing the three-dimensional spatial coordinate data for the digital model, a digital elevation model that can describe the three-dimensional geometric characteristics of the granite specimen after blasting was generated. The entire process of constructing the model and creating the digital elevation model is shown in Fig. 11.

To accurately analyze the morphological characteristics of the blast craters in the granite specimens under different confining pressures, a three-dimensional digital elevation cloud map was generated from the point cloud coordinate data collected via three-dimensional laser scanning. A Cartesian spatial coordinate system using point cloud coordinate data collected via three-dimensional laser scanning was set up by taking the center point of the charge as the zero

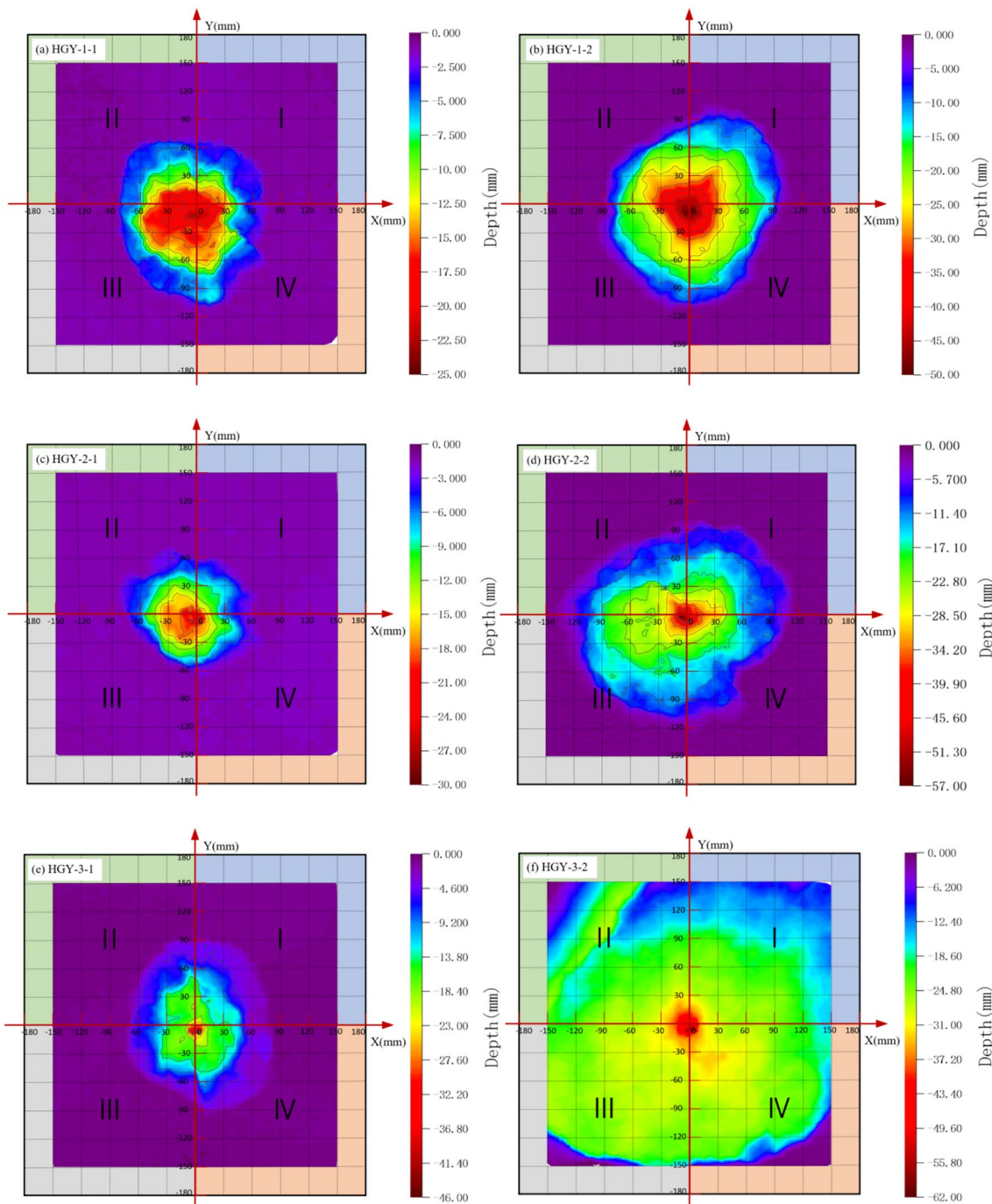


Fig. 12 Three-dimensional scanning digital elevation cloud maps of the blast craters in the granite specimens

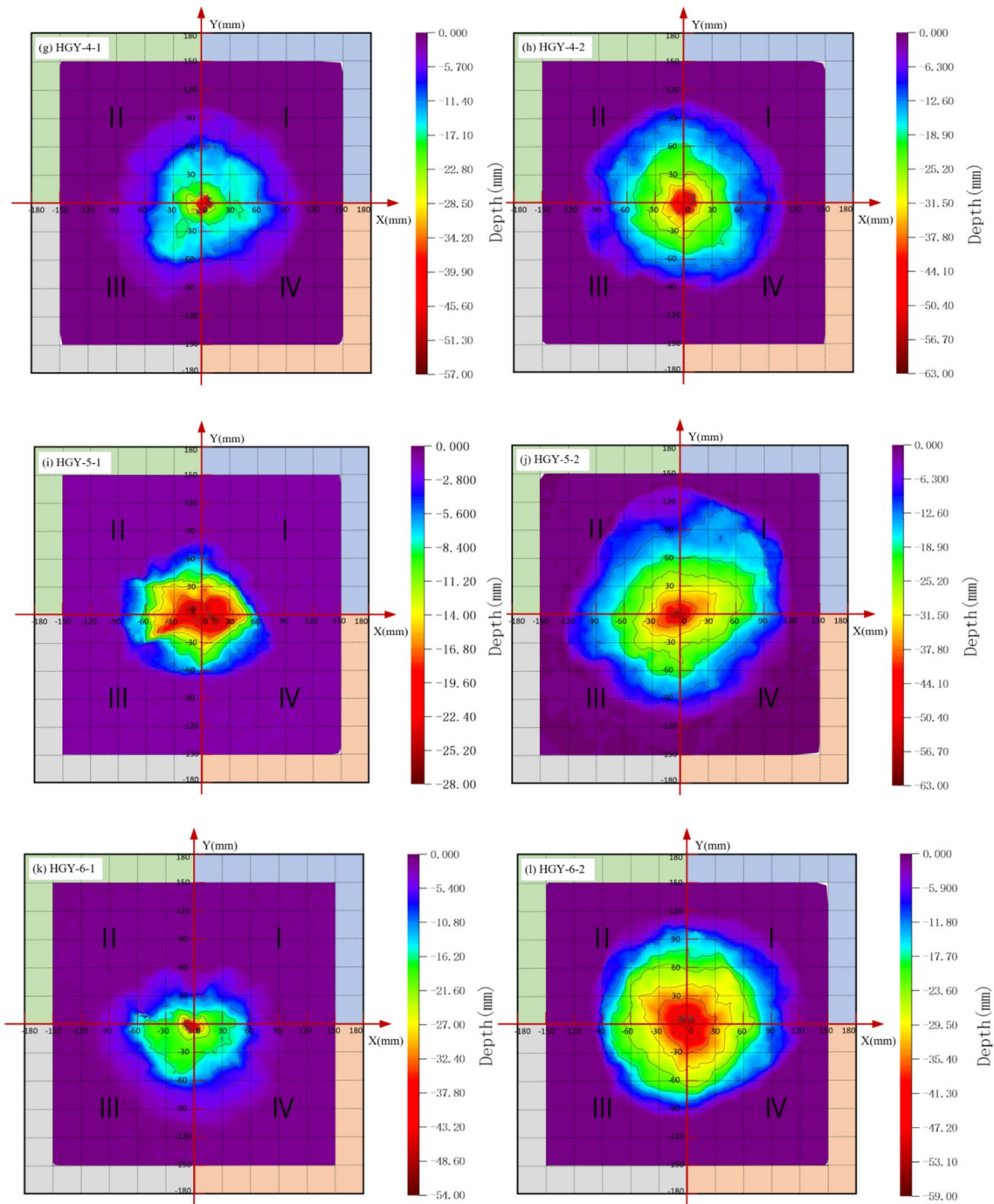


Fig. 12 (continued)

point, the surface of the charge as the XOY plane, and the specimen's length, width, and depth as the x -axis, y -axis, and z -axis, respectively. Then, the digital elevation cloud images of the positive and negative surfaces of all of the granite specimens were divided into four quadrants, namely, *I*, *II*, *III*, and *IV* (Fig. 12), to investigate the influence of the confining pressure on the morphology of the blast crater. In Fig. 12, the color scale corresponds to the depth of the crater.

Based on the typical failure morphology characteristics of the granite specimens after the explosion presented in Fig. 8 and the three-dimensional scanning digital elevation cloud maps of the granite specimens presented in Fig. 12, the macroscopic failure morphologies of the explosion craters in the granite specimens were comprehensively analyzed.

When both the horizontal and vertical stresses were zero, the two surfaces of the specimen exploded to form craters

with approximately circular shapes (Fig. 8a, b). It can also be seen from the digital elevation cloud map that the distribution of the failure depth in each quadrant was more uniform under a confining pressure of 0 MPa (Fig. 12a, b). With increasing vertical stress (comparison of HGY-1, HGY-2, and HGY-3), the range of the damage to the front of the granite specimen initially decreased and then increased (Fig. 8a, c, e), while the range damage to the back of the specimen gradually increased (Fig. 8b, d, f). The reason for this is that after the test, there were obvious structural planes (Fig. 8f). Under the working conditions of granite specimen HGY-3, the spalling boundary was smooth, and the fracture extended to the interior of the granite, which resulted in the range of the damage to the back surface being much larger than that under the other working conditions after the explosion. Under confining pressures of 8 MPa in the vertical direction and 0 MPa in the horizontal direction, the fracture developed along the direction of the compressive stress, indicating that the failure morphology of the granite was related to the stress conditions and the natural defects in the granite. It can similarly be seen from Fig. 12f that there was a clear fracture in the second quadrant, which resulted in spalling of blocks of the granite to form a huge blast crater.

For the working conditions for HGY-3, HGY-4, and HGY-6, the vertical stress was 8 MPa, and the horizontal stress values were 0 MPa, 4 MPa, and 8 MPa, respectively. The damaged area on the front of the granite specimen initially increased and then decreased (Fig. 8e, g, k), while the damaged area on the back initially decreased and then increased (Fig. 8f, h, l). It can also be seen from the cloud diagrams that the depth of the spalling platform in the front of the granite specimen (Fig. 12e, g, k) gradually deepened. That is, in the case when the vertical stress remained unchanged, as the horizontal stress increased, the degree and depth of the explosive spalled granite blocks increased. Since the damaged area on the back of granite specimen HGY-3 was influenced by the internal structural surface, the total damaged area was much larger than those in the other cases. Therefore, the variations in the size of the damaged area and the depth of the ladder-shaped fracture zone on the back of the granite under different confining pressures need to be discussed further.

Regarding the working conditions for HGY-1, HGY-5, and HGY-6, the vertical stress and horizontal stress were the same under all three working conditions, i.e., 0 MPa, 4 MPa, and 8 MPa, respectively. The range of the damage zone on the front of the granite specimen initially decreased and then increased (Fig. 8a, i, k), while the range of the damage zone on the back initially increased and then decreased (Fig. 8b, j, l). Under the action of equal biaxial static stress, the entire damaged area remained almost circular with increasing stress (Fig. 8b, j, l), and the crater depth distribution in each quadrant was more uniform (Fig. 12b, j, l).

In summary, under the combined effect of the explosion stress wave and bursting gas, under all the conditions, obvious blast craters formed; and under the different confining pressure conditions, the sizes, shapes, and positions of the bursting craters were quite different. The characteristics of the craters in the front and back surfaces of the specimens were also different under the same set of working conditions. For all the specimens, the area and depth of the crater in the front were smaller than those of the crater in the back. Through analysis of the failure morphology of the blast crater in the granite, the influence of the confining pressure on the morphology of the blast crater was directly observed. However, it was impossible to directly determine the influence of the different confining pressures on the law of explosion cratering for the same size charge using only macroscopic morphology analysis. Therefore, it was necessary to extract and analyze the parameters of the blast craters to further study the influence of the confining pressure on the characteristics of the blast craters.

3.4 Analysis of Characteristic Parameters of Cratering of Granite by an Explosion

The digital elevation model shows the three-dimensional morphology of the blast crater in the granite. Through post-processing of the digital elevation model, the relevant characteristic parameters of the crater in the granite after blasting were extracted and calculated (each parameter was measured based on the front and back surfaces of the granite specimen), including the maximum depth H_{\max} , average depth H_{ave} , length of the crater in the X direction L , width of the crater in the Y direction W , equivalent diameter of the crater D_h , surface area of the crater A_h , and volume of the crater V_h .

Based on the 3-D digital model of the explosion crater, a reference plane that coincides with the free surface of the specimen was created. Thus

$$A_i = \frac{1}{2} |\overline{AB} \times \overline{AC}| \quad (1)$$

$$A_s = \sum_{i=1}^n A_i. \quad (2)$$

In Eqs. (1) and (2), \overline{AB} and \overline{AC} are the vectors of any two edges of a single triangular mesh, and \times is the vector cross product; A_i is the area of a single triangular mesh; and A_s is the area of the portion where the free surface coincides with the reference plane.

Therefore, the area of the damaged zone on the free surface of the granite, A_h , is

$$A_h = A - A_s, \quad (3)$$

Fig. 13 3-D model of an explosion crater

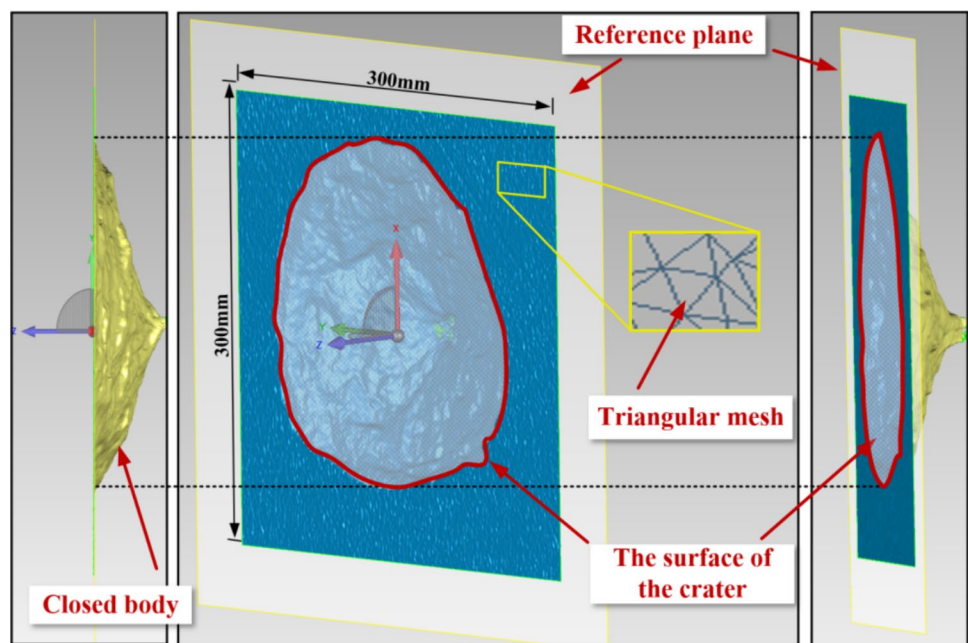
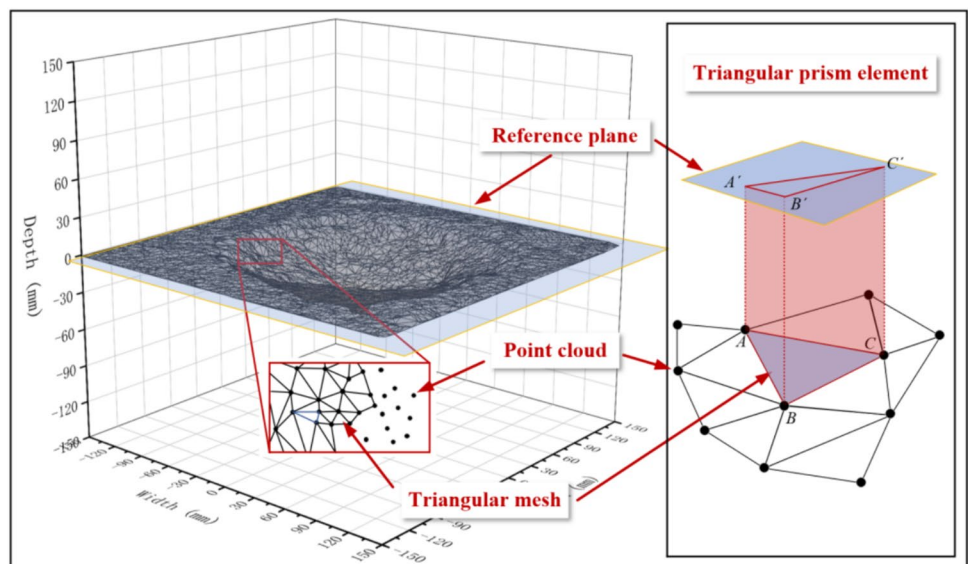


Fig. 14 Schematic diagram of the calculation of the volume of the crater



where A is the total area of the free surface of the 3-D model, $A = 300 \times 300 \text{ (mm}^2\text{)}$.

As shown in Fig. 13, the reference plane and the inner surface of the crater form a closed body, and the volume of this closed body is the volume of the crater. The volume was calculated using the projection method. By projecting each triangular mesh of the inner surface of the crater onto the reference plane to construct pentagonal micro-elements, the volume of the crater defined as the sum of the volumes of these micro-elements (Fig. 14).

When the triangular meshes are sufficiently small ($n \rightarrow \infty$), the area of the triangular meshes approaches the area of their projections onto the reference plane. At this point, the volume of the closed body can be considered to be composed of n triangular prism micro-elements. Thus

$$V_i = A_i h_i \tag{4}$$

$$V_h = \sum_{i=1}^n V_i, \tag{5}$$

where h_i is the height of the micro-element; V_i is the volume of the micro-element; and V_h is the total volume of the crater.

The average depth of the crater H_{ave} is the ratio of the volume V_h of the crater to the surface area of the crater A_h

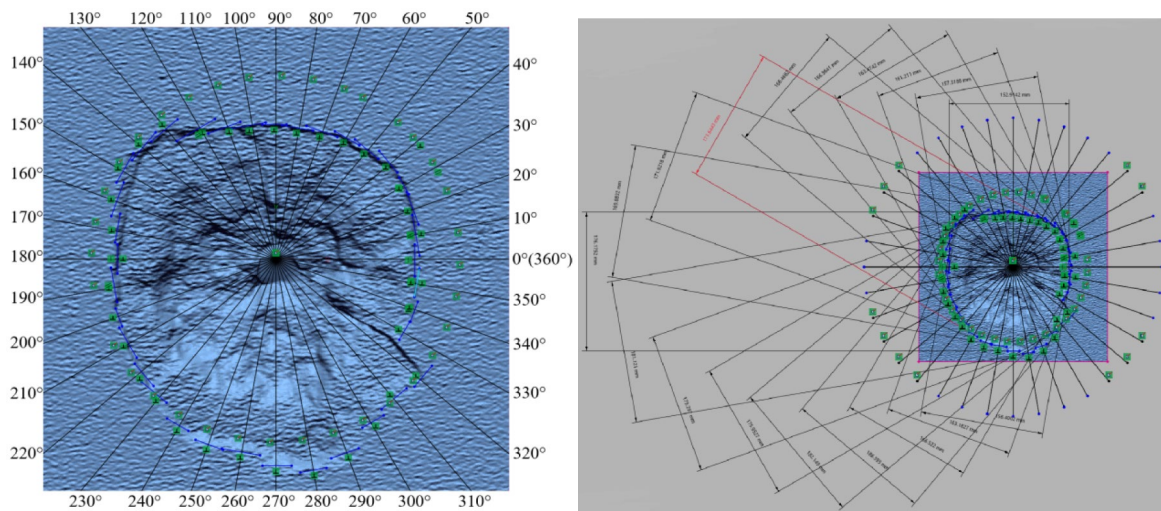


Fig. 15 Process of extracting the diameter of the crater in different directions

Table 3 Characteristic parameters of the craters in the granite specimens after blasting

No.	Specimen	H_{max} (mm)	H_{ave} (mm)	L (mm)	W (mm)	D_h (mm)	A_h (mm ²)	V_h (mm ³)
1	HGY-1-1	24.614	8.632	152.914	176.175	169.388	22,535.003	194,514.3
2	HGY-1-2	48.397	15.390	192.753	207.287	203.010	32,368.779	498,152.9
3	HGY-2-1	30.033	6.833	140.835	123.754	135.163	14,348.547	98,038.2
4	HGY-2-2	56.527	13.540	251.233	227.389	229.102	41,223.766	558,173.7
5	HGY-3-1	45.820	7.725	149.954	175.943	168.392	22,270.704	172,038.4
6	HGY-3-2	61.046	28.097	438.405	479.430	446.010	156,235.515	4,389,765.0
7	HGY-4-1	57.771	7.928	217.767	200.671	210.463	34,789.179	275,819.9
8	HGY-4-2	62.442	13.028	221.514	207.871	216.046	36,659.284	477,593.0
9	HGY-5-1	27.938	8.134	162.414	151.135	157.646	19,518.977	158,761.5
10	HGY-5-2	62.492	14.469	241.411	255.485	247.076	47,945.812	693,713.6
11	HGY-6-1	53.931	8.364	198.083	166.036	182.655	26,203.016	219,167.3
12	HGY-6-2	58.751	17.016	225.955	217.922	223.861	39,359.317	669,731.4

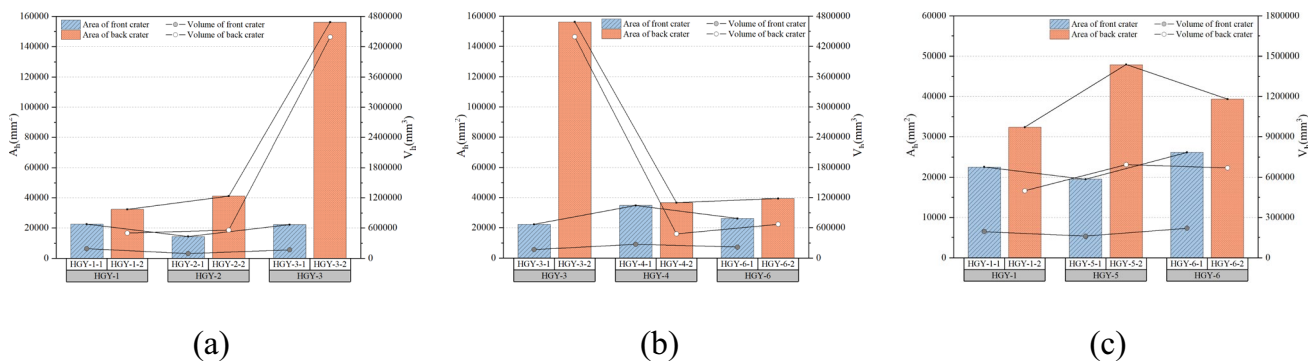


Fig. 16 The area and volume of the craters in the front and back surfaces of the granite under different working conditions. **a** different vertical confining pressures, **b** different horizontal confining pressures, and **c** different equal biaxial stresses

$$H_{ave} = \frac{V_h}{A_h} \tag{6}$$

The average diameter D_h was determined by averaging the diameters of the craters in different directions with the blast-hole as the center point and 10° as the interval. A schematic diagram of the calculation is shown in Fig. 15

$$D_h = \frac{\sum_{k=1}^n r_k}{n} \quad (n = 18), \tag{7}$$

where $\sum_{k=1}^n r_k$ is the sum of the crater radii at 10° intervals starting from 0° .

The characteristic dimensions of all of the specimens after blasting are summarized in Table 3.

3.4.1 Volume and Area

The volume of the crater and the area of the free surface are the main morphological characteristics of the crater. Figure 16 shows the volume of the crater and the area of the free surface crushing zone in the front and back surfaces of the granite specimens under different working conditions. As can be seen from Fig. 16a, in the vertical direction, with increasing confining pressure, the volume and failure area of the crater in the back of the granite increased. The front blasthole in the granite was filled with C30 quick-setting concrete. Its strength is quite different from that of the rock,

and the cohesive force between the concrete and rock surface was much lower than that between the adjacent granite masses. Therefore, part of the energy generated by the explosion destroyed the bond between the concrete and granite. As the concrete plug lost strength and was thrown out, more energy escaped through the blasthole, resulting in little difference between the front fracture surface area and the volume of the crater under different confining pressures. In comparison, the back of the granite was more significantly affected by the peripheral pressure as it was an unperforated hole, and thus, the energy generated by the explosion was fully utilized in the rock-crushing process. It was observed that the vertical static stress significantly affected the crater volume and the area of the failure zone on the free surface. It can be seen from Fig. 16b that under a static stress of 8 MPa in the vertical direction, the volume of the crater in the back of the granite and the area of the free surface failure zone decreased with increasing horizontal pressure. This shows that the horizontal pressure not only restricted the expansion of the damage zone at the free surface but also limited the effect of the crushing of the rock under the same charge. Due to the increase in the horizontal pressure, stress concentration occurred around the blasthole in the front of the granite, which had a positive effect on the crushing of the rock under the action of the explosion. When the stress reached 8 MPa, the equal biaxial stress inhibited the fragmentation of the sample. Therefore, the volume of the crater and the area of the crushing zone initially increased and then decreased.

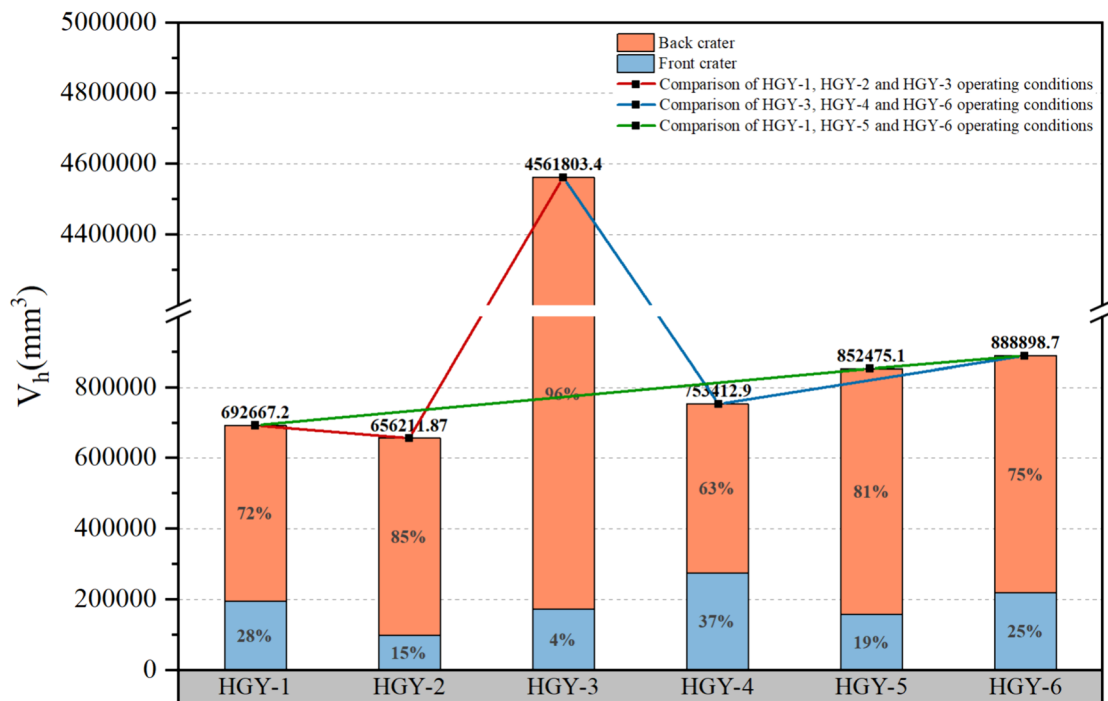


Fig. 17 The total volume of the granite damaged under the various working conditions

Figure 16c shows that under equal biaxial stress, the front and back of the granite underwent different failure patterns. With increasing biaxial stress, the volume of the crater and the area of the free surface crushing zone on the front side of the granite initially decreased and then increased, indicating that the low static stress had an inhibitory effect on the crushing of the granite, while the higher biaxial static stress increased the stress concentration around the blasthole and played a significant role in promoting the crushing and fracturing of the granite. The volume of the crater in the back of the granite and the area of the free surface crushing zone both initially increased and then decreased, indicating that the higher biaxial static stress inhibited the crushing of the granite. Figure 16 shows that, for the same charge, the crater volume V_h and the final crushing area A_h of the free surface exhibited the same change trends under different static stress states. This indicates that there was no obvious change in the morphology of the crater, and there was a certain proportional relationship between V_h and A_h .

Figure 17 shows the total volumes of the granite specimens that failed under the various working conditions. Through analysis, it was determined that because we used the non-through hole drilling method, the initial centrosymmetric explosion acceleration field and energy field were changed during the explosion process, resulting in asymmetric development of the front and back explosion craters. More energy leaked out of the blasthole. As a result, an average of 79% of the total volume of the explosion craters in the front and back surfaces of the granite under different working conditions was accounted for by the crater in the back, while only 21% was accounted for by the crater in the front. The total damage volume of the granite initially decreased and then increased with increasing vertical stress (red lines). When the longitudinal static stresses were both 8 MPa, the total volume of the granite damaged also initially decreased and then increased as the horizontal stresses increased (blue lines). This indicates that when the stresses in both directions were unequal, the lower stress inhibited the overall

failure of the granite, and as the stress increased further, it played a role in promoting failure of the granite specimen. Under equal biaxial stresses, the total volume of the granite damaged gradually increased with increasing confining pressure (green lines). This shows that the increase in the equal biaxial stress promoted the overall failure of the granite.

3.4.2 Width, Length, and Equivalent Diameter of Craters

It can be seen from Fig. 18a that with increasing vertical static stress, the morphological features of the free surface fracture zone of the two craters in the front and back of the granite tended to be larger in the Y -axis (W) direction than in the X -axis (L) direction. Based on analysis of Fig. 12, it was concluded that the fracture zone exhibited a distinct elliptical morphology with increasing vertical static stress, and the long-axis direction of the ellipse was the direction of the application of the static stress. This indicates that under the action of vertical static stress, the area of the explosion craters not only gradually increased with increasing static stress but also affected the morphological characteristics of the surface crushing zone. Figure 18b shows that when the vertical static stress was 8 MPa, the difference between the width and length of the free surface damage zone gradually decreased with increasing horizontal pressure, and the morphological characteristics gradually changed from elliptical to nearly circular (Fig. 12). This indicates that the biaxial stress not only inhibited the expansion of the squeezed zone on the free surface but also significantly affected its morphology. Under the action of equal biaxial stress, the width and length of the free surface fracture zone in the front and back of the granite were approximately the same (Fig. 18c). As can be seen from the three-dimensional digital scanning height cloud map (Fig. 12) of the crater in the granite specimen, the cloud maps for HGY-1, HGY-5, and HGY-6 are more evenly distributed in the four quadrants of the coordinate system. The craters all exhibited approximately circular morphological characteristics. As can be seen from Figs. 16

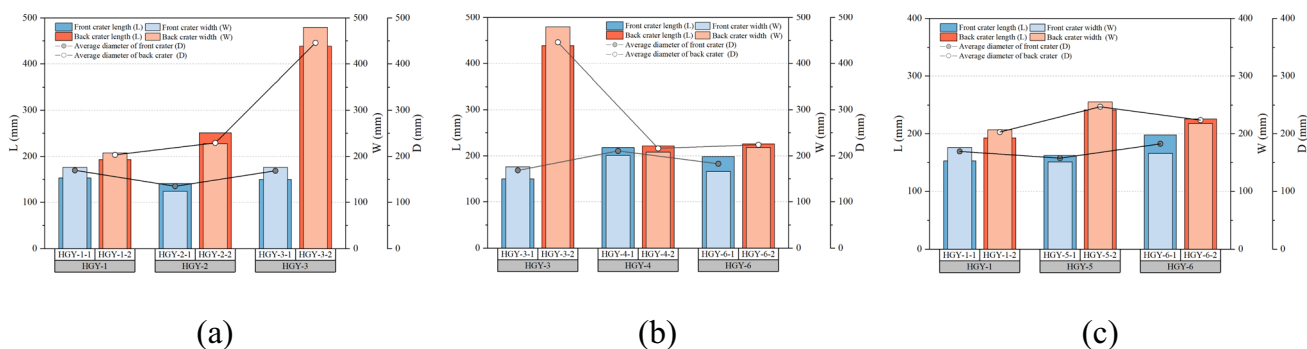


Fig. 18 The widths, lengths, and equivalent diameters of the craters in the granite specimens under the different working conditions. **a** Different vertical confining pressures, **b** different horizontal confining pressures, and **c** different equal biaxial stresses

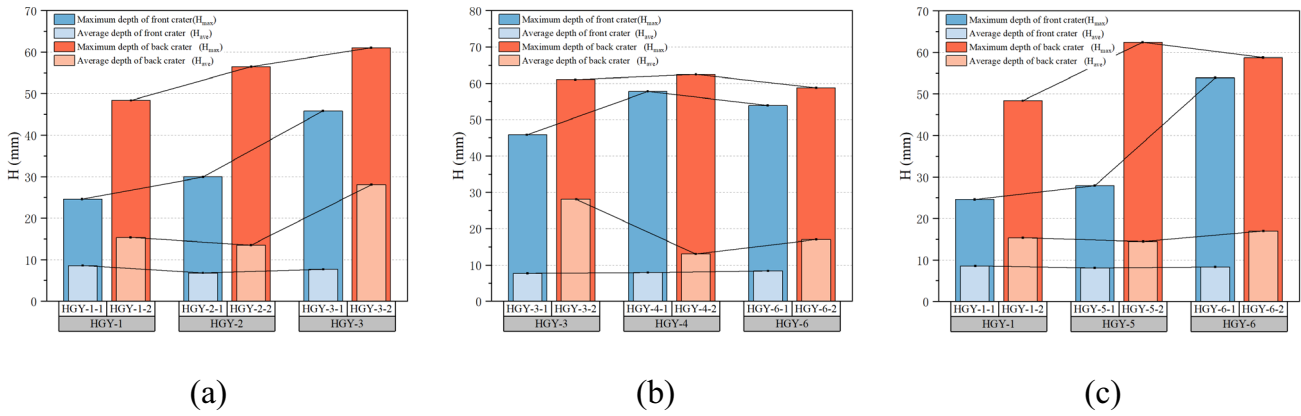


Fig. 19 The maximum depth and average depth of the granite craters under the different working conditions. **a** Different vertical confining pressures, **b** different horizontal confining pressures, and **c** different equal biaxial stresses

and 18, the variation trends of the area, width, length, and equivalent diameter of the crater in the granite were highly consistent under the different working conditions. Since the equivalent diameter D_h was calculated from the length L and width W (Eq. (1)), the characteristic parameters L , W , D_h , and A_h of the explosion crater in the granite exhibited a certain correlation.

3.4.3 Maximum Depth and Average Depth

The average depth was calculated using Eq. (2). It can be seen from Fig. 19a that with increasing vertical static stress, the maximum depth of the blast craters in the front and back of the granite increased. The average depth (H_{ave}) exhibits less fluctuation, and its change trend is relatively smooth. Based on analysis of Figs. 16 and 18, as the vertical static stress increased, the depth, volume, and free surface crushing area of the crater increased synchronously with a certain ratio, and the craters also exhibited similar morphological characteristics (Fig. 9). When the static stress in the vertical direction was 8 MPa, the maximum depth of the crater in

the front of the granite initially increased and then decreased with increasing horizontal pressure (Fig. 19b). This trend was almost consistent with the change trends of the crater volume, free surface crushing area, width, length, and equivalent diameter. It was also concluded that with increasing horizontal stress, the depth, volume, and free surface of the crater increased synchronously with a certain ratio. It can also be seen from Fig. 19b that the average depth of the crater in the front of the granite exhibited a stable trend, which also proves the correctness of the above analysis. The maximum depth of the blast crater in the back of the granite also initially increased and then decreased. However, due to the existence of the internal structural surface of the granite under the working conditions for HGY-3, the range of the damage to the back of the specimen under the action of the explosion was much larger than those under the other working conditions, so the average depth of the explosion crater initially decreased and then gradually stabilized. As can be seen from Fig. 19c, under the action of equal biaxial stress, the maximum depth of the blast crater, the volume of the blast crater, and the area, width, length, and equivalent

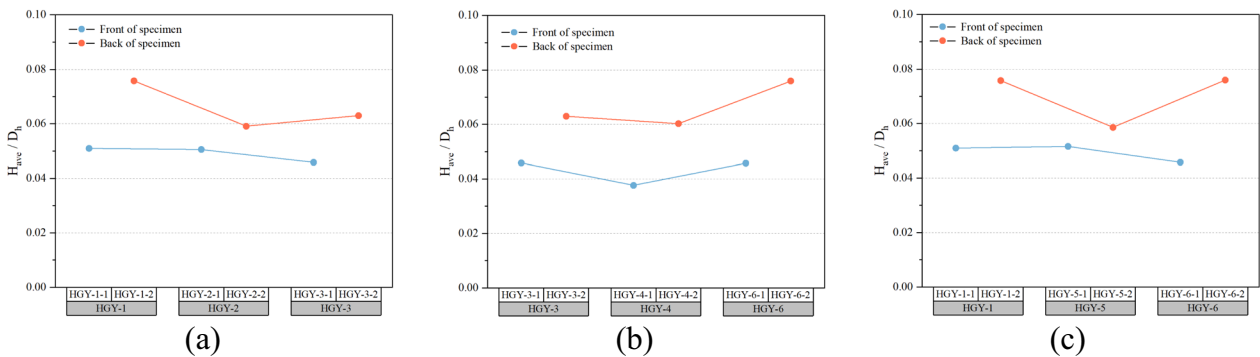


Fig. 20 Ratio of average depth to equivalent diameter. **a** different vertical confining pressures, **b** different horizontal confining pressures, and **c** different equal biaxial stresses

diameter of the free surface fracture zone on the front and back of the granite also exhibited consistent trends, and the trend of the average depth was stable.

In summary, under different the confining pressure conditions, the depth of the crater in the granite under an explosion load was consistent with the trends of the area, width, length, and equivalent diameter of the free surface fracture zone. The depth, volume, and area of the free surface fracture zone of the crater changed synchronously with a certain ratio, and the profile morphology of the crater was always a flat funnel-like shape with ladder-shaped fracture patterns.

3.4.4 Ratio of Average Depth to Equivalent Diameter

Figure 20 presents plots of the ratio of the average depth to the equivalent diameter of the craters formed by an explosion under the different working conditions. Under the different stress conditions, the H_{ave}/D_h ratio varies smoothly and always fluctuates between 0.04 and 0.08. This trend further indicates that parameters such as the crater depth, volume, free surface crushing area, and equivalent diameter varied synchronously according to a certain ratio. It can also be seen from Fig. 20 that the equivalent diameter of the crater was much larger than the average depth of the crater, so the profile of the crater exhibited a flat funnel-like shape.

3.4.5 Ratio of Average Depth to Equivalent Diameter

The coefficient of variation (CV) can eliminate the influence of scale and dimension differences between different characteristic parameters, allowing for analysis of the variation characteristics of the parameters of the craters in the granite specimens under different confining pressures. This enabled quantitative assessment of the sensitivity of the crater shape parameters to changes in the confining pressure. Figure 21 shows the variation coefficients of the crater parameters under different confining pressures, which were calculated using Eq. (8)

$$CV = \frac{\sigma}{\mu} \times 100\% \tag{8}$$

In Eq. (8), σ is the standard deviation of the data, and μ is the mean of the data.

Figure 21a shows the variation coefficients of the crater parameters under a transverse pressure of 0 MPa as the longitudinal pressure changed from 0 to 4 MPa and then to 8 MPa. Due to the increase in the axial pressure, the variation coefficients of the volumes of the craters in the front and back of the granite were the highest (31.2% and 118.2%, respectively), followed by the crater area (21.5% and 85.5%, respectively). This indicates that the volume and area of the crater were highly sensitive to changes in the confining pressure, and the increase in the uniaxial confining pressure significantly affected the variations in the volume and area of the crater. For the crater in the back, the maximum crater depth exhibited the lowest sensitivity to changes in the confining pressure, with a variation coefficient of 10.9%. This suggests that for a fixed explosive charge, the change in the axial confining pressure had a limited impacted on the maximum crater depth. The crater width (variation coefficient of 47.8%) was the primary factor that led to the high sensitivity of the area and volume of the crater to the confining pressure. It was found that the increase in the uniaxial confining pressure also had a significant impact on the planar shape of the crater. For the front crater, the maximum crater depth (variation coefficient of 32.9%) was the main factor contributing to the high sensitivity of the volume of the crater to the confining pressure. Figure 21b shows the variation coefficients of the crater parameters under a longitudinal pressure of 8 MPa, when the transverse pressure was changed from 0 to 4 MPa and then to 8 MPa. Under an initial confining pressure of 8 MPa, the maximum depths of the craters in the front and back had the lowest sensitivity to the changes in the confining pressure, with variation coefficients of 8% and

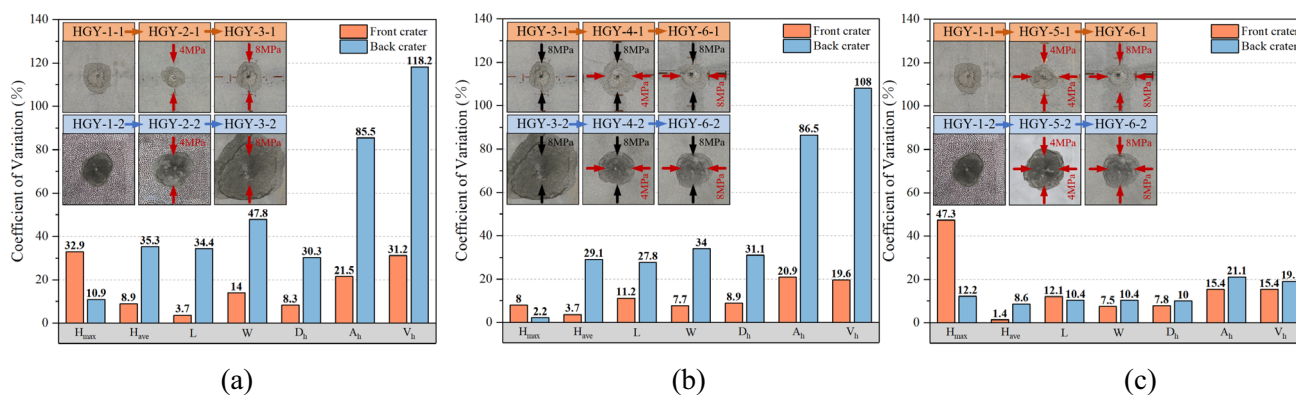


Fig. 21 The coefficients of variation (CV) of the crater parameters under different confining pressures

2.2%, respectively. The increase in the transverse confining pressure significantly affected the changes in the lengths of the craters in the front and back (variation coefficients of 11.2% and 27.8%, respectively), making it the primary factor causing the high sensitivity of the area and volume of the crater to the confining pressure. Figure 21c shows the variation coefficients of the crater parameters as the biaxial stress changed from 0 to 4 MPa and then to 8 MPa. Compared to the uniaxial confining pressure changes, the variation coefficients of the crater parameters were lower for increasing biaxial confining pressure. This indicates that the biaxial confining pressure had a more uniform and stable influence on the crater morphology parameters compared to the uniaxial confining pressure.

4 Conclusions

In this study, we conducted indoor chemical explosion tests on large granite specimens under different confining pressures. The failure process, damage morphology characteristics, and variation patterns of the large granite specimens under different stress states were analyzed using techniques such as high-speed photography, 3-D scanning measurement, and 3-D model construction. The main conclusions of this study are as follows.

The explosion cratering process of the large granite specimens consisted of spalling from the inside to the outside. An obvious radial tensile crack did not form in the initial phase of the explosion, but the specimen bulged, which produced circumferential cracks. Based on the macroscopic characteristics, the crater failure mode of the granite specimens was divided into three stages: the crushing failure stage, circumferential fracturing stage, and stepped fracture stripping stage. The microfracture surface of the granite exhibited a stepped fracture structure with sharp fracture edges, and the fracture surface exhibited obvious directionality.

In this study, compared with the traditional measurement method, a damage characterization method that utilizes three-dimensional scanning technology and digital model construction technology was developed. Our method includes four stages: point cloud data acquisition, data noise reduction, surface fitting, and model construction. Accurate measurement of the characteristic parameters of the crater is realized by constructing a three-dimensional digital model. The digital elevation cloud map generated based on the three-dimensional coordinate data of the point cloud can be used to intuitively characterize the location, range, size, and depth of the damage after the explosion.

There were significant differences in the variation trends of the characteristics of the explosion craters in

the granite specimens under different confining pressure conditions. The vertical stress significantly affected the volume of the crater and the area of the damage zone on the free surface of the granite, and they exhibited a positive correlation. The damage zone exhibited an elliptical morphology, and the direction of the static stress was the same as the direction of the longitudinal axis. When the vertical stress was fixed, the horizontal stress played an inhibiting role in the failure of the back surface of the granite, the width and length of the failure zone gradually decreased, and the difference between the width and length of the damage zone also gradually decreased. The morphological characteristics of the crater in the damage zone also gradually changed from elliptical to approximately circular. Under the action of equal biaxial stresses, a low static stress promoted crushing of the granite, while a high static stress inhibited the crushing of the back of the granite. The volume of the crater and the area of the crushing zone initially increased and then decreased.

Under the combined effects of different confining pressures and blast loading, the depth of the crater and the area, width, length, and equivalent diameter of the free-face crushed zone in the granite exhibited consistent trends. The H_{ave}/D_h ratio changed smoothly, and the parameters, such as the crater depth, volume, free fracture area, and equivalent diameter, changed synchronously with a certain ratio. The equivalent diameter of the crater was much larger than the average depth of the crater, and the profile of the crater exhibited a flat funnel-like shape with ladder-shaped fracture patterns.

Acknowledgements The financial support provided by the National Natural Science Foundation of China (Grant Nos. 11532013 and 11872157) is sincerely appreciated. The authors thank LetPub (www.letpub.com) for its linguistic assistance during the preparation of this manuscript.

Author Contributions All of the authors contributed to the conception and design of the study. Zhenqing Wang and Yongsheng established the overarching research goals. Jiazheng Gao carried out experimental investigations, as well as data processing and analysis, while Yeqing Chen and Chunhai Li jointly supervised the experiments. The first draft of the manuscript was written by Jiazheng Gao, and all of the authors commented on previous versions of the manuscript. All of the authors have read and approved of the final manuscript.

Funding The financial support provided by the National Natural Science Foundation of China (Grant Nos. 11532013 and 11872157) is sincerely appreciated.

Data Availability The data that support the findings of this study are available from the corresponding author upon reasonable request.

Declarations

Conflict of interest The authors declare that we have no financial and personal relationships with other people or organizations that can inappropriately influence our work. There is no professional or other personal interest of any nature or kind in any product, services, and/

or company that could be construed as influencing the position presented in, or the review of the manuscript entitled *Experimental Study of Failure and Morphology of Large Granite Specimens Under Different Confining Pressures and Blast Loading*.

Consent to Participate Not applicable.

Consent to Publish Not applicable.

Ethics Approval Not applicable.

References

- Ai T, Wu S, Zhang R et al (2021) Changes in the structure and mechanical properties of a typical coal induced by water immersion. *Int J Rock Mech Min Sci* 138:104597. <https://doi.org/10.1016/j.ijrmmms.2020.104597>
- Alner GJ, Araújo HM, Arnison GJ et al (2005) Limits on WIMP cross-sections from the NAIAD experiment at the Boulby Underground Laboratory. *Phys Lett B* 616:17–24. <https://doi.org/10.1016/j.physletb.2000.09.001>
- Bear J (1975) Dynamics of fluids in porous media. *Soil Sci* 120:162–163. <https://doi.org/10.1097/00010694-197508000-00022>
- Chazal V, Brissot R, Cavaignac JF et al (1998) Neutron background measurements in the Underground Laboratory of Modane. *Astropart Phys* 9:163–172. [https://doi.org/10.1016/S0927-6505\(98\)00012-7](https://doi.org/10.1016/S0927-6505(98)00012-7)
- Chen Y-L, Wang S-R, Ni J et al (2017) An experimental study of the mechanical properties of granite after high temperature exposure based on mineral characteristics. *Eng Geol* 220:234–242. <https://doi.org/10.1016/j.enggeo.2017.02.010>
- Chen P, Liu C, Wang Y (2018a) Size effect on peak axial strain and stress-strain behavior of concrete subjected to axial compression. *Constr Build Mater* 188:645–655. <https://doi.org/10.1016/j.conbuilmat.2018.08.072>
- Chen S, Walske ML, Davies IJ (2018b) Rapid mapping and analyzing rock mass discontinuities with 3-D terrestrial laser scanning in the underground excavation. *Int J Rock Mech Min Sci* 110:28–35. <https://doi.org/10.1016/j.ijrmmms.2018.07.012>
- Cheng Y, Zhang Y, Yu Z et al (2020) An investigation on hydraulic fracturing characteristics in granite geothermal reservoir. *Eng Fract Mech* 237:107252. <https://doi.org/10.1016/j.engfracmech.2020.107252>
- Chi LY, Zhang ZX, Aalberg A et al (2019a) Fracture processes in granite blocks under blast loading. *Rock Mech Rock Eng* 52:853–868. <https://doi.org/10.1007/s00603-018-1620-0>
- Chi LY, Zhang Z-X, Aalberg A et al (2019b) Measurement of shock pressure and shock-wave attenuation near a blast hole in rock. *Int J Impact Eng* 125:27–38. <https://doi.org/10.1016/j.ijimpeng.2018.11.002>
- Exadaktylos GE, Vardoulakis I (2001) Microstructure in linear elasticity and scale effects: a reconsideration of basic rock mechanics and rock fracture mechanics. *Tectonophysics* 335:81–109. [https://doi.org/10.1016/s0040-1951\(01\)00047-6](https://doi.org/10.1016/s0040-1951(01)00047-6)
- Fan L, Gao J, Du X, Wu Z (2020a) Spatial gradient distributions of thermal shock-induced damage to granite. *J Rock Mech Geotech Eng* 12:917–926. <https://doi.org/10.1016/j.jrmge.2020.05.004>
- Fan LF, Gao JW, Du XL (2020b) Thermal cycling effects on micro-property variation of granite by a spatial micro-observation. *Rock Mech Rock Eng* 53:2921–2928. <https://doi.org/10.1007/s00603-020-02065-8>
- Feng G-L, Feng X-T, Chen B-R, Xiao Y-X (2015) Microseismic sequences associated with rockbursts in the tunnels of the Jinping II hydropower station. *Int J Rock Mech Min Sci* 80:89–100. <https://doi.org/10.1016/j.ijrmmms.2015.06.011>
- Gao J, Xi Y, Fan L, Du X (2021) Real-time visual analysis of the microcracking behavior of thermally damaged granite under uniaxial loading. *Rock Mech Rock Eng* 54:6549–6564. <https://doi.org/10.1007/s00603-021-02639-0>
- Goel MD, Matsagar VA (2014) Blast-resistant design of structures. *Pract Period Struct Des Constr* 19:04014007. [https://doi.org/10.1061/\(asce\)sc.1943-5576.0000188](https://doi.org/10.1061/(asce)sc.1943-5576.0000188)
- Gong QM, Yin LJ, Wu SY et al (2012) Rock burst and slabbing failure and its influence on TBM excavation at headrace tunnels in Jinping II hydropower station. *Eng Geol* 124:98–108. <https://doi.org/10.1016/j.enggeo.2011.10.007>
- Guo LQ, Huang YX, Huang JB (2012) Experimental study on anisotropy of granite residual soil. *Adv Mater Res* 518–523:4721–4725. <https://doi.org/10.4028/www.scientific.net/AMR.518-523.4721>
- Guo Y, Han Z, Guo H et al (2019) Numerical simulation damage analysis of pipe-cement-rock combination due to the underwater explosion. *Eng Fail Anal* 105:584–596. <https://doi.org/10.1016/j.engfailanal.2019.07.029>
- Hagan TN (1979) Rock breakage by explosives. *Acta Astronaut* 6:329–340. [https://doi.org/10.1016/0094-5765\(79\)90102-4](https://doi.org/10.1016/0094-5765(79)90102-4)
- He C, Yang J (2018a) Laboratory study of dynamic mechanical characteristic of granite subjected to confining pressure and cyclic blast loading. *Lat Am J Solids Struct* 15:e44. <https://doi.org/10.1590/1679-78254424>
- He C, Yang J (2018b) Dynamic crack propagation of granite subjected to biaxial confining pressure and blast loading. *Lat Am J Solids Struct* 15:e45. <https://doi.org/10.1590/1679-78254463>
- He C, Yang J, Yu Q (2018) Laboratory study on the dynamic response of rock under blast loading with active confining pressure. *Int J Rock Mech Min Sci* 102:101–108. <https://doi.org/10.1016/j.ijrmmms.2018.01.011>
- He C, Gao J, Chen D, Xiao J (2020) Investigation of stress wave interaction and fragmentation in granite during multihole blastings. *IEEE Access* 8:185187–185197. <https://doi.org/10.1109/access.2020.3030253>
- He C, Chen D, Xiao J et al (2021) Experimental study of crack propagation and failure around a horseshoe tunnel during nearby blasting. *Int J Rock Mech Min Sci* 139:104628. <https://doi.org/10.1016/j.ijrmmms.2021.104628>
- Hu SR, Peng JC, Huang C et al (2011) An overview of current status and progress in coal mining of the deep over a kilometer. *China Min Mag* 20:105–110. <https://doi.org/10.3969/j.issn.1004-4051.2011.07.027>
- Hudson JA, Crouch SL, Fairhurst C (1972) Soft, stiff and servo-controlled testing machines: a review with reference to rock failure. *Eng Geol* 6:155–189. [https://doi.org/10.1016/0013-7952\(72\)90001-4](https://doi.org/10.1016/0013-7952(72)90001-4)
- Jung W-J, Utagawa M, Ogata Y et al (2001) Effects of rock pressure on crack generation during tunnel blasting. *Kayaku Gakkaishi J Jpn Explos Soc* 62:138–146
- Kao S, Zhao G, Xu W et al (2020) Experimental study of the association between sandstone size effect and strain rate effect. *J Mech Sci Technol* 34:3597–3608. <https://doi.org/10.1007/s12206-020-0811-2>
- Kulatilake PHSW, Wu Q, Yu Z, Jiang F (2013) Investigation of stability of a tunnel in a deep coal mine in China. *Int J Min Sci Technol* 23:579–589. <https://doi.org/10.1016/j.ijmst.2013.07.018>
- Kutter HK, Fairhurst C (1971) On the fracture process in blasting. *Int J Rock Mech Min Sci Geomech Abstr* 8:181–202. [https://doi.org/10.1016/0148-9062\(71\)90018-0](https://doi.org/10.1016/0148-9062(71)90018-0)

- Lan H, Martin CD, Hu B (2010) Effect of heterogeneity of brittle rock on micromechanical extensile behavior during compression loading. *J Geophys Res Solid Earth* 115:2009JB006496. <https://doi.org/10.1029/2009jb006496>
- Lesko KT (2009) The deep underground science and engineering laboratory at homestake. *J Phys Conf Ser* 173:012005. <https://doi.org/10.1088/1742-6596/173/1/012005>
- Li S, Feng X-T, Li Z et al (2012) In situ monitoring of rockburst nucleation and evolution in the deeply buried tunnels of Jinping II hydropower station. *Eng Geol* 137–138:85–96. <https://doi.org/10.1016/j.enggeo.2012.03.010>
- Li X, Gong F, Tao M et al (2017) Failure mechanism and coupled static-dynamic loading theory in deep hard rock mining: a review. *J Rock Mech Geotech Eng* 9:767–782. <https://doi.org/10.1016/j.jrmge.2017.04.004>
- Lippmann-Pipke J, Erzinger J, Zimmer M et al (2011) Geogas transport in fractured hard rock—correlations with mining seismicity at 3.54km depth, TauTona gold mine, South Africa. *Appl Geochem* 26:2134–2146. <https://doi.org/10.1016/j.apgeochem.2011.07.011>
- Lisitsyn IV, Inoue H, Nishizawa I et al (1998) Breakdown and destruction of heterogeneous solid dielectrics by high voltage pulses. *J Appl Phys* 84:6262–6267. <https://doi.org/10.1063/1.368946>
- Liu J, Ma T, Liu Y et al (2018) History, advancements, and perspective of biological research in deep-underground laboratories: a brief review. *Environ Int* 120:207–214. <https://doi.org/10.1016/j.envint.2018.07.031>
- Lu ZX, Feng ZC, Zhao YS (2007) Influence of rock inhomogeneity on strength-size effect of rock materials. *J China Coal Soc* 32:917–920. <https://doi.org/10.3321/j.issn:0253-9993.2007.09.005>
- Masoumi H, Saydam S, Hagan PC (2016) Unified size-effect law for intact rock. *Int J Geomech* 16:04015059. [https://doi.org/10.1061/\(asce\)gm.1943-5622.0000543](https://doi.org/10.1061/(asce)gm.1943-5622.0000543)
- Meng Q, Zhang M, Han L et al (2016) Effects of size and strain rate on the mechanical behaviors of rock specimens under uniaxial compression. *Arab J Geosci* 9:527. <https://doi.org/10.1007/s12517-016-2559-7>
- Miuchi K, Minowa M, Takeda A et al (2003) First results from dark matter search experiment with LiF bolometer at Kamioka underground laboratory. *Astropart Phys* 19:135–144. [https://doi.org/10.1016/s0927-6505\(02\)00192-5](https://doi.org/10.1016/s0927-6505(02)00192-5)
- Nordyke MD (1961) Nuclear craters and preliminary theory of the mechanics of explosive crater formation. *J Geophys Res* 1896–1977(66):3439–3459. <https://doi.org/10.1029/JZ066i010p03439>
- Parisi ME, Brino L, Gilli P et al (2017) La Maddalena exploratory tunnel. *Geomech Tunn* 10:265–274. <https://doi.org/10.1002/geot.201700011>
- Peng J, Wong LNY, Teh CI, Li Z (2018) Modeling micro-cracking behavior of bukit timah granite using grain-based model. *Rock Mech Rock Eng* 51:135–154. <https://doi.org/10.1007/s00603-017-1316-x>
- Peng J, Zhang F, Yan G et al (2019) Experimental study on rock-like materials fragmentation by electric explosion method under high stress condition. *Powder Technol* 356:750–758. <https://doi.org/10.1016/j.powtec.2019.09.001>
- Peng J, Zhang F, Du C, Yang X (2020a) Effects of confining pressure on crater blasting in rock-like materials under electric explosion load. *Int J Impact Eng* 139:103534. <https://doi.org/10.1016/j.ijimpeng.2020.103534>
- Peng J, Zhang F, Yang X (2020b) Dynamic fracture and fragmentation of rock-like materials under column charge blasting using electrical explosion of wires. *Powder Technol* 367:517–526. <https://doi.org/10.1016/j.powtec.2020.04.012>
- Qi C, Wang M, Wang Z, Li X (2023) Study on the coupling effect of sample size and strain rate on rock compressive strength. *Rock Mech Rock Eng* 56:5103–5114. <https://doi.org/10.1007/s00603-023-03309-z>
- Ranjith PG, Zhao J, Ju M et al (2017) Opportunities and challenges in deep mining: a brief review. *Engineering* 3:546–551. <https://doi.org/10.1016/j.eng.2017.04.024>
- Roszkowski L, Sessolo EM, Trojanowski S (2018) WIMP dark matter candidates and searches—current status and future prospects. *Rep Prog Phys* 81:066201. <https://doi.org/10.1088/1361-6633/aab913>
- Rustan AP (1998) Micro-sequential contour blasting—how does it influence the surrounding rock mass? *Eng Geol* 49:303–313. [https://doi.org/10.1016/s0013-7952\(97\)00062-8](https://doi.org/10.1016/s0013-7952(97)00062-8)
- Saiang D (2010) Stability analysis of the blast-induced damage zone by continuum and coupled continuum–discontinuum methods. *Eng Geol* 116:1–11. <https://doi.org/10.1016/j.enggeo.2009.07.011>
- Sharma M, Bishnoi S (2019) The interfacial transition zone: microstructure, properties, and its modification. In: Rao ARM, Ramanjaneyulu K (eds) Recent advances in structural engineering, vol 2. Springer, Singapore, pp 745–754
- Sher EN, Mikhailov AM, Chernikov AG (2011a) Brittle failure zone size under the concentrated charge blasting near free surface. *J Min Sci* 47:734–740. <https://doi.org/10.1134/s1062739147060050>
- Wang Z-L, Li Y-C, Shen RF (2007) Numerical simulation of tensile damage and blast crater in brittle rock due to underground explosion. *Int J Rock Mech Min Sci* 44:730–738. <https://doi.org/10.1016/j.ijrmms.2006.11.004>
- Wang M, Qiu Y, Yue S (2018) Similitude laws and modeling experiments of explosion cratering in multi-layered geotechnical media. *Int J Impact Eng* 117:32–47. <https://doi.org/10.1016/j.ijimpeng.2017.11.018>
- Wei M-D, Dai F, Xu N-W et al (2017) An experimental and theoretical assessment of semi-circular bend specimens with chevron and straight-through notches for mode I fracture toughness testing of rocks. *Int J Rock Mech Min Sci* 99:28–38. <https://doi.org/10.1016/j.ijrmms.2017.09.004>
- Weibull W (1939) A statistical theory of the strength of materials. Generalstabens litografiska anstalts förlag
- Weibull W (2013) Fatigue testing and analysis of results. Elsevier
- Wu SC, Guo C, Gao YT et al (2021) Discussion and prospect of source location of rock fracture. *Yanshilixue Yu Gongcheng Xuebao* 40:874–891. <https://doi.org/10.13722/j.cnki.jrme.2020.0710>
- Wu H, Zhao G, Ma S (2022) Failure behavior of horseshoe-shaped tunnel in hard rock under high stress: Phenomenon and mechanisms. *Trans Nonferrous Met Soc China* 32:639–656. [https://doi.org/10.1016/s1003-6326\(22\)65822-9](https://doi.org/10.1016/s1003-6326(22)65822-9)
- Xia Y, Lin M, Liao L et al (2014) Fractal characteristic analysis of fragments from rockburst tests of large-diameter specimens. *Yanshilixue Yu Gongcheng Xuebao Chin J Rock Mech Eng* 33:1358–1365
- Xie LX, Zhang QB, Gu JC et al (2019) Damage evolution mechanism in production blasting excavation under different stress fields. *Simul Model Pract Theory* 97:101969. <https://doi.org/10.1016/j.simpat.2019.101969>
- Xie H, Li C, He Z et al (2021) Experimental study on rock mechanical behavior retaining the in situ geological conditions at different depths. *Int J Rock Mech Min Sci* 138:104548. <https://doi.org/10.1016/j.ijrmms.2020.104548>
- Yan P, Zhao Z, Lu W et al (2015) Mitigation of rock burst events by blasting techniques during deep-tunnel excavation. *Eng Geol* 188:126–136. <https://doi.org/10.1016/j.enggeo.2015.01.011>
- Yan F, Lin B, Zhu C et al (2016) Using high-voltage electrical pulses to crush coal in an air environment: an experimental study. *Powder Technol* 298:50–56. <https://doi.org/10.1016/j.powtec.2016.05.023>
- Yan F, Xu J, Lin B et al (2019) Changes in pore structure and permeability of anthracite coal before and after high-voltage electrical pulses treatment. *Powder Technol* 343:560–567. <https://doi.org/10.1016/j.powtec.2018.11.083>

- Yang L-Y, Ding C-X (2018) Fracture mechanism due to blast-imposed loading under high static stress conditions. *Int J Rock Mech Min Sci* 107:150–158. <https://doi.org/10.1016/j.ijrmms.2018.04.039>
- Yang J, Chen W, Zhao W et al (2017) Geohazards of tunnel excavation in interbedded layers under high in situ stress. *Eng Geol* 230:11–22. <https://doi.org/10.1016/j.enggeo.2017.09.007>
- Yang L, Ding C, Yang R et al (2018) Full field strain analysis of blasting under high stress condition based on digital image correlation method. *Shock Vib* 2018:1–7. <https://doi.org/10.1155/2018/4894078>
- Yang L, Yang A, Chen S et al (2021) Model experimental study on the effects of in situ stresses on pre-splitting blasting damage and strain development. *Int J Rock Mech Min Sci* 138:104587. <https://doi.org/10.1016/j.ijrmms.2020.104587>
- Yi C, Johansson D, Greberg J (2018) Effects of in-situ stresses on the fracturing of rock by blasting. *Comput Geotech* 104:321–330. <https://doi.org/10.1016/j.compgeo.2017.12.004>
- Yilmaz O, Unlu T (2014) An application of the modified holmberg–persson approach for tunnel blasting design. *Tunn Undergr Space Technol* 43:113–122. <https://doi.org/10.1016/j.tust.2014.04.009>
- Zaitsev YB, Wittmann FH (1981) Simulation of crack propagation and failure of concrete. *Matér Constr* 14:357–365. <https://doi.org/10.1007/BF02478729>
- Zhang F, Peng J, Qiu Z et al (2017) Rock-like brittle material fragmentation under coupled static stress and spherical charge explosion. *Eng Geol* 220:266–273. <https://doi.org/10.1016/j.enggeo.2017.02.016>
- Zhang S, Wang L, Gao M (2019) Experimental investigation of the size effect of the mode I static fracture toughness of limestone. *Adv Civ Eng* 2019:1–11. <https://doi.org/10.1155/2019/7921694>
- Zhang S, Wang H, Li X et al (2021) Experimental study on development characteristics and size effect of rock fracture process zone. *Eng Fract Mech* 241:107377. <https://doi.org/10.1016/j.engfracmech.2020.107377>
- Zhao G, Wang D, Gao B, Wang S (2017) Modifying rock burst criteria based on observations in a division tunnel. *Eng Geol* 216:153–160. <https://doi.org/10.1016/j.enggeo.2016.11.014>

Publisher's Note Springer Nature remains neutral with regard to jurisdictional claims in published maps and institutional affiliations.

Springer Nature or its licensor (e.g. a society or other partner) holds exclusive rights to this article under a publishing agreement with the author(s) or other rightsholder(s); author self-archiving of the accepted manuscript version of this article is solely governed by the terms of such publishing agreement and applicable law.